EES Solar

REVIEW

View Article Online
View Journal | View Issue

Cite this: *EES Sol.*, 2025, **1**, 219

Recent progress in covalent organic frameworks as heterogeneous photocatalysts for photochemical conversion

Xiangyu Zhang,†[ac] Rufan Chen,†[a] Yongxiang Zhou,[ac] Zekun Chen,[ac] Guo Qin Xu[ac] and Qing-Hua Xu*[abc]

Received 11th January 2025
Accepted 13th April 2025

DOI: 10.1039/d5el00003c

rsc.li/EESSolar

Covalent organic frameworks (COFs) are a class of porous and crystalline materials constructed from covalently linked building blocks. Over the past decade, dramatic progress has been made in synthesizing new COFs with diverse applications, especially in photocatalysis. In this review, we highlight recent progress in COFs as heterogeneous photocatalysts for their applications toward hydrogen evolution from water splitting, carbon dioxide reduction, organic transformations, and hydrogen peroxide production. We focus on rational design of COF structures as well as our understanding of interplay between COF structures and their optical properties as efficient heterogeneous photocatalysts. Challenges and perspectives are discussed at the end.

Broader context

The quest for sustainable energy solutions has driven transformative advances in light harvesting and conversion technologies over the past five decades. Solar energy utilization has evolved from simple photon absorption to complicated photocatalytic systems that can efficiently capture, convert, and store light energy. Beginning with fundamental studies of light–matter interactions in semiconductor photocatalysts, the field has progressed through several breakthrough innovations in controlling light absorption, charge separation, and surface reactions. The development of new materials has revolutionized our ability to harness the solar spectrum – from traditional semiconductors that are limited to UV light to advanced covalent organic frameworks (COFs) capable of efficient visible light utilization. Most significantly, advances in the design and synthesis of COFs have enabled unprecedented control over light-harvesting efficiency, charge separation and transport processes, and catalytically active sites. The emergence of precisely engineered COFs has marked a critical convergence of structural order and photophysical functionality, establishing new paradigms for solar energy conversion. These developments have accelerated progress across multiple frontiers, from artificial photosynthesis to solar fuel production, laying the foundation for next-generation technologies that can effectively convert sunlight into chemical energy for practical applications.

1 Introduction

Fossil fuels have been the main source of energy for economic development since the industrial revolution. The release of greenhouse gases from massive consumption of these natural resources has caused lots of environmental problems and created lots of concerns and demand for alternative energy resources.[1–3] Solar energy has been considered as the most promising alternative energy resource as it is sustainable, clean, and low-cost. To be utilized for practical applications, solar energy needs to be coupled with energy collection, conversion and storage processes.[4] In nature, green plants convert solar energy into chemical energy by utilization of sunlight as the driving force and enzymes as photocatalysts to transform carbon dioxide and water into carbohydrates and oxygen, offering excellent inspiration for researchers to develop efficient artificial photocatalytic systems.[5,6]

In 1972, Fujishima and Honda reported the pioneering work on titanium dioxide (TiO_2) as a photocatalyst to realize water splitting under irradiation with ultraviolet (UV) light in a photoelectrochemical cell.[7] Since then, photocatalysis has been applied to various reactions with a focus on the development of low-cost, stable and highly efficient photocatalysts. Many traditional inorganic semiconductors have been explored as photocatalysts for photo-induced production of chemical fuels and value-added compounds. However, their narrow light absorption range resulted in poor harvesting of solar energy.[8,9] Organic semiconductors such as carbon nitrides, conjugated microporous polymers (CMPs), linear conjugated polymers and covalent triazine-based frameworks (CTFs) have recently emerged as promising materials for photocatalytic applications.[10–13] The light absorption and band structure of these organic semiconductors can be tuned by modular copolymerization strategies. However, their amorphous or

[a]National University of Singapore (Suzhou) Research Institute, Suzhou 215123, China
[b]College of Science, Eastern Institute of Technology, Ningbo 315200, China
[c]Department of Chemistry, National University of Singapore, 117543, Singapore. E-mail: qhxu@eitech.edu.cn/chmxqh@nus.edu.sg
† Equally contributed to this work.

semicrystalline structures would still hinder charge transportation and consequently limit their photoactivity.[14]

The development of novel porous and crystalline materials such as metal–organic frameworks (MOFs), covalent organic frameworks (COFs) and hydrogen-bonded organic frameworks (HOFs) has opened up new possibilities for new types of highly efficient photocatalysts.[15–20] MOFs and HOFs are constructed *via* coordination bonds and hydrogen bonding interactions, respectively. Both of them usually exhibit relatively low chemical stability and thus limit their applications.[21,22] COFs are a class of polymers that are constructed from molecular building blocks with strong covalent bonds through condensation reactions.[23–25] They are particularly interesting as they combine properties of crystallinity, permanent porosity, synthetic versatility and good physical/chemical stability.[26–30] The long-range-ordered structure of COFs is beneficial for photo-induced electron transport to the catalyst surface for photocatalytic applications. Furthermore, the diverse selection of chromophores enables tunable absorption and band structures. COFs have integrated the advantages of the above-mentioned organic semiconductors while overcoming their limitations at the same time.[31,32]

Since the first report of a semiconducting COF in 2008,[33] numerous efforts have been devoted to the field of COF assisted hydrogen evolution from water splitting,[34] photocatalytic carbon dioxide (CO_2) reduction[35] and organic transformations.[36] In this review, we will mainly discuss structural design strategies for the construction of efficient COFs as heterogeneous photocatalysts (Scheme 1). The relationship between structural design and optoelectronic properties will be discussed in detail for different photocatalytic applications. Perspectives of challenges and possible directions for future research will be discussed in the end.

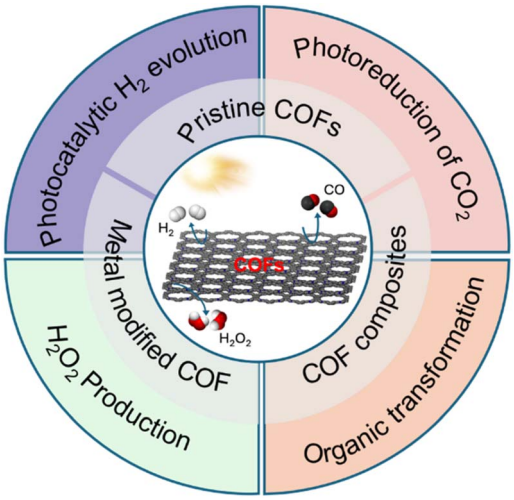

Scheme 1 Schematic illustration of the diverse photocatalytic applications of COF-based heterogeneous photocatalysts.

2 Structural aspects – fundamentals of COFs for photocatalysis

2.1 Structure design of COFs for photocatalysis

Porous and crystalline COFs can be obtained by topological utilization of building blocks through covalent bonds.[25] The topology diagram or geometry of monomers determines the dimensionality and spatial orientation of COF skeletons as well as the size and shape of their pores. Monomers with C_1, C_2, C_3, C_4 and C_6 symmetries have been used for the preparation of two-dimensional (2D) COFs with different topologies. The shapes of monomers and their major combination geometries are summarized in Fig. 1. The design strategy of one knot plus one linker is used most widely for the construction of 2D COFs to produce various backbones and pore channels. Besides that, a multicomponent strategy could allow more than one knot and linker to be integrated into one COF, which brings about more options for the design of different functional COFs.

Under the guidance of different topology diagrams, precursors of COFs condensed to form covalently linked layered skeletons and aligned pores. For the application of photocatalysis, favorable properties, such as excellent light-harvesting

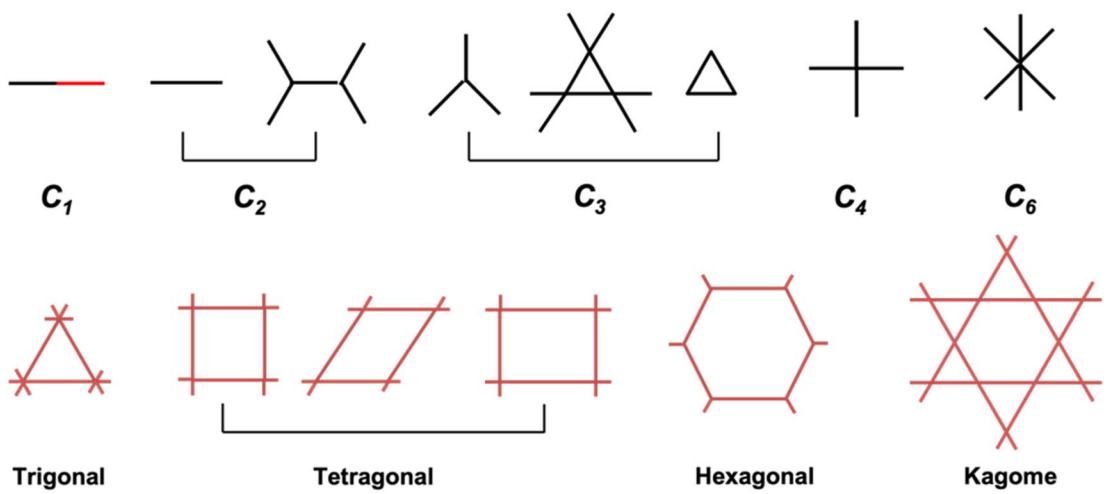

Fig. 1 Topological schematics guiding the design of 2D COFs.

ability, suitable band structure and efficient charge separation, all originate from the structures of COFs. Specifically, skeletons of COFs can be constructed to act as light-harvesters, binding sites, or redox centers by tailored design of numerous building blocks. The high structural porosity gives them high surface areas and permanent pores, enabling enhanced accessibility of sensitizers, sacrificial reagents and cocatalysts. Functional units have been linked *via* various linkage motifs into stable and conjugated scaffolds, which contribute to increased charge carrier mobility and superior stability to work under harsh conditions. Furthermore, the molecular stacking modes and distances of COFs have been utilized to tune their optical and electronic properties.[37–43] Periodically aligned columnar π-arrays can serve as light-harvesting matrices and offer pathways for charge carrier transport. Fully π-conjugated COFs with fully conjugated linkages offer charge transport pathways along with the perpendicular π-column directions. The pores or channels across the materials provide space for reactants to contact reaction centers while the products could be easily released from the catalytic sites.[44] Recently, 3D-COFs have attracted significant attention due to their exceptional photocatalytic capabilities. Similar to their 2D counterparts, topology engineering is crucial for the rational design of 3D COFs. Compared to 2D COFs, 3D COFs often demonstrate interconnected channels and large accessible surface areas, which significantly enhance catalytic performance. Moreover, controlling interpenetration and incorporating steric hindrance groups ensure structural robustness, optimizing active site exposure and enhancing catalytic stability.[45,46] Various 3D COFs with topologies such as stp, srs, and fcc have been reported as efficient photocatalysts. For instance, Ding *et al.* developed JUC-640-M COFs based on the stp topology, achieving ultra-large pores, record-low crystal density, and significantly enhanced CO_2 photoreduction performance.[47] Zhu *et al.* reported an innovative TMB-COF with srs topology, in which steric hindrance groups effectively convert planar precursors into spatially intricate frameworks, enhancing catalytic site availability.[48] Furthermore, Li *et al.* demonstrated the functionalization of 3D fcc COFs with benzene, pyrazine, and tetrazine groups, significantly tuning reaction microenvironments and boosting photocatalytic urea synthesis *via* improved electron–hole separation, enhanced light-harvesting, and reactant co-adsorption capabilities.[49] These sophisticated structural and functional designs position 3D COFs as promising platforms for high-performance photocatalytic applications.

Linkage selection significantly affects the properties of COFs.[50] The boric acid condensation reaction was the earliest reported method for synthesizing COFs. Subsequently, the imine condensation reaction emerged and has become the most widely utilized method, with more than half of all reported COFs synthesized *via* this route. Traditional imine-linked COFs offer simple synthesis, structural versatility, and good crystallinity, but often require carefully designed monomers or precursors. However, their moderate chemical stability limits practical applications, particularly under harsh photocatalytic conditions. To overcome this limitation, imine-derived linkages—such as β-ketoenamine, triazine, oxazole, and thiazole—have been developed through tandem or post-synthetic modification reactions, transforming imine bonds into more robust structures with improved chemical stability, enhanced structural order, and favorable charge-transfer properties crucial for photocatalysis.[51] Meanwhile, sp^2 carbon-linked COFs, synthesized *via* direct C=C condensation, achieve extended π-conjugation, superior electronic conductivity and significantly improved semiconductor properties,[52] which greatly enhance charge separation efficiency and boost photocatalytic performance.[53] Alternatively, hydrazone-linked COFs, derived from aldehyde and hydrazide precursors, possess exceptional hydrolytic stability, structural flexibility, abundant heteroatomic sites (N and O), and post-synthetic modification capabilities, which enhance intermolecular interactions, facilitate efficient charge-carrier separation, and present diverse catalytic sites, leading to further amplified photocatalytic efficiency.[54]

2.2 Advantages of COFs for photocatalysis

COFs are one of the most attractive organic semiconductors pertaining to heterogeneous photocatalysis, owing to several advantages (Fig. 2): (1) the tailorable structure endows COFs with foreseeable semiconducting properties and band structures, and the highest occupied molecular orbital (HOMO) and the lowest unoccupied molecular orbital (LUMO) levels of the COF materials could be fine-tuned through molecular design of the well-defined skeletons to tailor their light harvesting ability and semiconducting properties for photocatalytic applications. Also, by utilizing electron deficient or electron donating building blocks, the donor–acceptor structures have been widely used in the construction of COFs to offer enhanced separation efficiencies of electrons and holes. (2) Highly crystalized structure of COFs favors effective charge transfer, as the stacked regularly π-units form an extended framework with close interactions, thereby offering pathways for charge transfer across the material. The well defined structures of COFs also make it clearer to explore the relationship between the structure and photocatalytic activity. (3) The high surface area and porosity of COFs are beneficial not only for the interactions of active sites with the substrate, sacrificial reagent and cocatalyst, but also for effective diffusion during the photocatalytic process. (4) Strong covalent bonds give COFs high stability, especially chemical stability, which makes them resistant to hydrolysis, pH variations, and oxidative or reductive environments and allowing them to work over the long term. The linkage motif in COFs not only provides high stability, but can also be engineered to improve the conjugation in planes to facilitate the charge transfer process. Unlike traditional catalysts that often suffer from fast charge recombination (such as TiO_2 and carbon nitride), photocorrosion (such as CdS, In_2S_3, ZnCdS, and $ZnIn_2S_4$), a narrow wavelength range of harvesting light or limited surface area, COFs enhance photocatalytic performance through molecular-level design, allowing for better selectivity, higher quantum efficiency, and metal-free sustainability. In addition, their chemical stability, environmental friendliness, and potential for multi-functional applications (such as H_2 production, CO_2 reduction, and organic

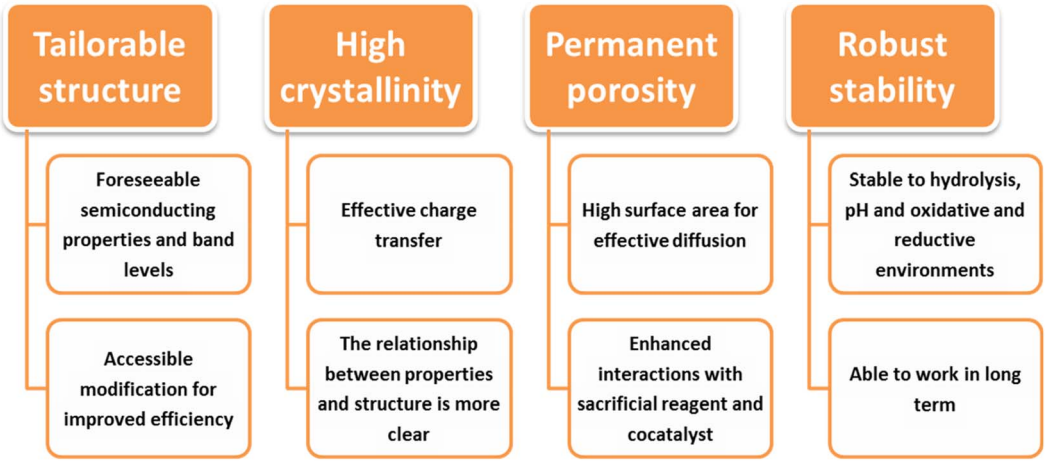

Fig. 2 Advantages of COFs for photocatalysis due to their unique properties.

transformations) make them promising next generation photocatalysts.

Metal doping and construction of heterojunctions are two very common and effective means to enhance photocatalytic performance. Metal ions and complexes could be bound dispersedly to the backbones of COFs through coordination interaction as new active sites.[55,56] The introduction of metals could also facilitate charge transfer and separation, leading to improved photocatalytic activity.[57–59] Some metal-modified COFs demonstrate superior photocatalytic performance even without requiring noble-metal co-catalysts, exhibiting excellent catalytic stability and long-term recyclability.[57] Metal sites anchored through the backbones of COFs provide exceptional interactions with substrates, thus amplifying the efficiency of photocatalysis. Recent studies have demonstrated that metal clusters integrated within COFs significantly improve local electron density, promote efficient exciton dissociation and thus enhance photoreduction efficiency. Furthermore, precise tuning of the metal environments with distinct coordination geometries reduces energy barriers for critical intermediate formation, resulting in improved catalytic selectivity and activity.[58,59] Metal-covalent organic frameworks (MCOFs) serve as a bridge between MOFs and COFs, combining the beneficial properties of both. They maintain the stability, porosity, and tunability of COFs and inherit the rich metal-coordination chemistry of MOFs, yielding frameworks with superior catalytic properties, stability, and multifunctionality. The tunable band structures of COFs are very convenient for them to combine with another semiconductor to construct different types of heterojunctions as the HOMO and LUMO levels of COFs could be easily adjusted for desired heterojunctions. More importantly, strong interactions of COFs with organic or inorganic semiconductors are vital for charge transfer within the heterojunction.

3 Applications in photocatalysis

A typical photocatalytic reaction starts with absorption of light to generate electron–hole pairs, followed by charge separation and transportation to the surface for the oxidation/reduction reactions. Consequently, efforts to enhance the solar energy conversion efficiency of photocatalysts primarily focus on three key areas: improving strength and broadening the spectral range of light absorption, optimizing charge separation and transfer, and accelerating surface reactions. To ensure that photo-excited electrons and holes possess sufficient redox potential to drive surface reactions, the LUMO of covalent organic frameworks must be positioned at a more negative potential than the redox potential of the reduction reaction (Fig. 3). Concurrently, the HOMO should be situated at a more positive potential than the redox potential of the oxidation reaction. COFs provide a unique approach for the application of photocatalysis thanks to their interesting chemical and physical properties such as harvesting of broadband light and efficient charge separation and transfer.[60] Recent research progress in COFs in various applications such as photocatalytic hydrogen evolution, carbon dioxide reduction, organic transformations and hydrogen peroxide production will be summarized in this part.

3.1 Photocatalytic H_2 evolution

Photocatalytic hydrogen evolution (PHE) from water splitting involves a series of photochemical events and it is key to optimize these events to achieve optimum performance.[61] This requires the design of various interfaces to enable continuous flow of electrons and holes to drive the reaction. However, it lacks a general principle for designing organic systems to interlock multiple interfaces to seamlessly integrate light absorption, exciton splitting, charge transfer and transport processes. As COFs enable a systematic design of the skeleton and pores, it is highly possible to engineer various interfaces into one framework. Prior to elucidating specific examples, we have compiled an overview of the PHE performance of various COF-based photocatalysts (Table 1).

3.1.1 Pristine COFs. Hydrazone linked TFPT-COF is the first example of a COF to act as a photocatalyst for hydrogen evolution from water splitting.[62] TFPT-COF was constructed by

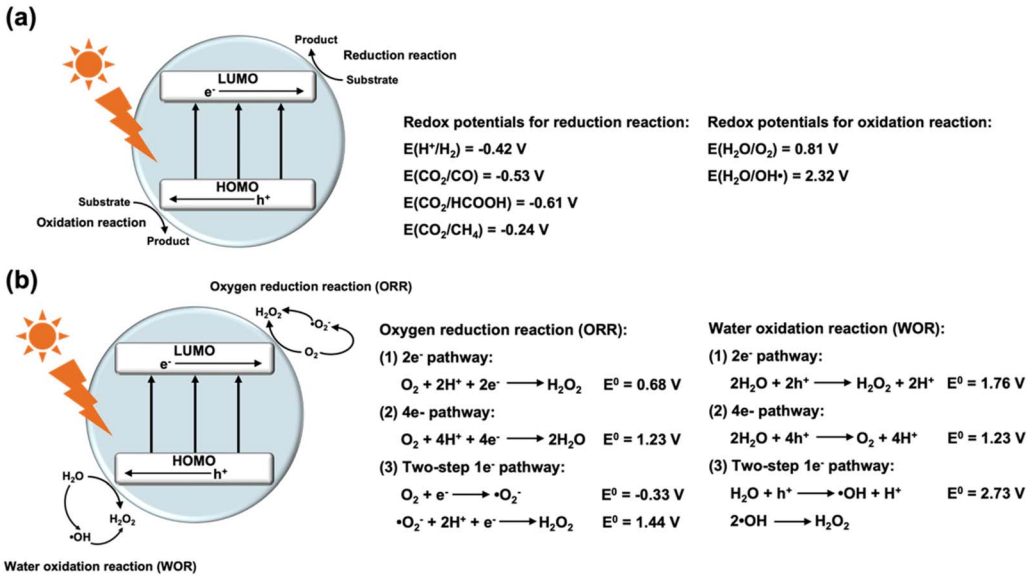

Fig. 3 Schematic illustration of the processes of photocatalytic water splitting, carbon dioxide reduction (a) and hydrogen peroxide production (b), and corresponding redox potentials of the relevant reactions.

the condensation reaction of 1,3,5-tris(4-formyl-phenyl)triazine (TFPT) and 2,5-diethoxy-terephthalohydrazide. Under irradiation with visible light, PHE rates of 230 μmol h^{-1} g^{-1} and 1.97 mmol h^{-1} g^{-1} were achieved in the presence of a Pt co-catalyst by using sodium ascorbate and triethanolamine (TEOA) as the sacrificial donor, respectively. A distinct feature of

Table 1 Summary of H_2 evolution rates of COF-based photocatalysts

Samples	Irradiation conditions	Sacrificial agent	Co-catalyst	HER rate (μmol h^{-1} g^{-1})	Ref.
TFPT-COF	$\lambda > 420$ nm	TEOA	Pt	1970	62
N_3-COF	$\lambda > 420$ nm	TEOA	Pt	1703	63
ZnPor-DETH-COF	$\lambda > 400$ nm	TEOA	Pt	413	64
PyTz-COF	AM 1.5	Ascorbic acid	Pt	2072.4	65
TCDA-COF	780 nm > λ > 420 nm	Ascorbic acid	Pt	70 800	66
TpPa-COF-$(CH_3)_2$	$\lambda > 420$ nm	Sodium ascorbate	Pt	8330	67
sp^2c-COF_{ERDN}	$\lambda > 420$ nm	TEOA	Pt	2120	68
PY-DHBD-COF	$\lambda > 420$ nm	Ascorbic acid	Pt	42 432	69
COF–alkene	$\lambda > 420$ nm	TEOA	Pt	2330	70
v-2D-COF-NO1	$\lambda > 400$ nm	TEOA	Pt	1970	71
sp^2c-COF-ST	$\lambda > 420$ nm	TEOA	Pt	2150	72
sp^2c-Py-BT COF	$\lambda > 420$ nm	—	NA	573	73
TtaTfa	$\lambda > 420$ nm	Ascorbic acid	Pt	20 700	74
COF-954	780 nm > λ > 420 nm	Ascorbic acid	Pt	137 230	75
CYANO-CON	$\lambda > 420$ nm	Ascorbic acid	Pt	134 200	76
2D-TP-PB	$\lambda > 420$ nm	TEOA	Pt	24 980	77
g-$C_{18}N_3$-COF	$\lambda > 420$ nm	Ascorbic acid	Pt	292	78
Cu-salphen-HDCOF-NSs	$\lambda > 420$ nm	TEA	Cu	36 990	79
Co_9S_8@COF	$\lambda > 420$ nm	Ascorbic acid	Co_9S_8	23 150	80
Zn@H-TpPa	$\lambda > 420$ nm	Sodium ascorbate	Pt	28 000	81
COF-Cu_3TG	λ = 380–800 nm	—	NA	10 470	82
TiO_2-TpPa-1-COF (1 : 3)	$\lambda > 420$ nm	Sodium ascorbate	Pt	11 190	83
T-COF@CdS-3	Full spectrum	Ascorbic acid	Pt	12 500	84
COF-42	AM 1.5G	TEOA	Cobaloxime	163	85
NH_2-UiO-66/TpPa-1-COF (4 : 6)	$\lambda > 420$ nm	Sodium ascorbate	Pt	23 410	86
ATNT-4	$\lambda > 420$ nm	Ascorbic acid	Pt	14 228.1	87
TBTA/g-C_3N_4	$\lambda > 420$ nm	Ascorbic acid	Pt	26 040	88
PEG@BT-COF	$\lambda > 420$ nm	Ascorbic acid	Pt	11 140	89
MAC-FA1/S-COF	$\lambda > 420$ nm	Ascorbic acid	NA	100 000	90
COF316/Pt@TpBpy-COF	$\lambda > 420$ nm	—	Pt	220.4	91

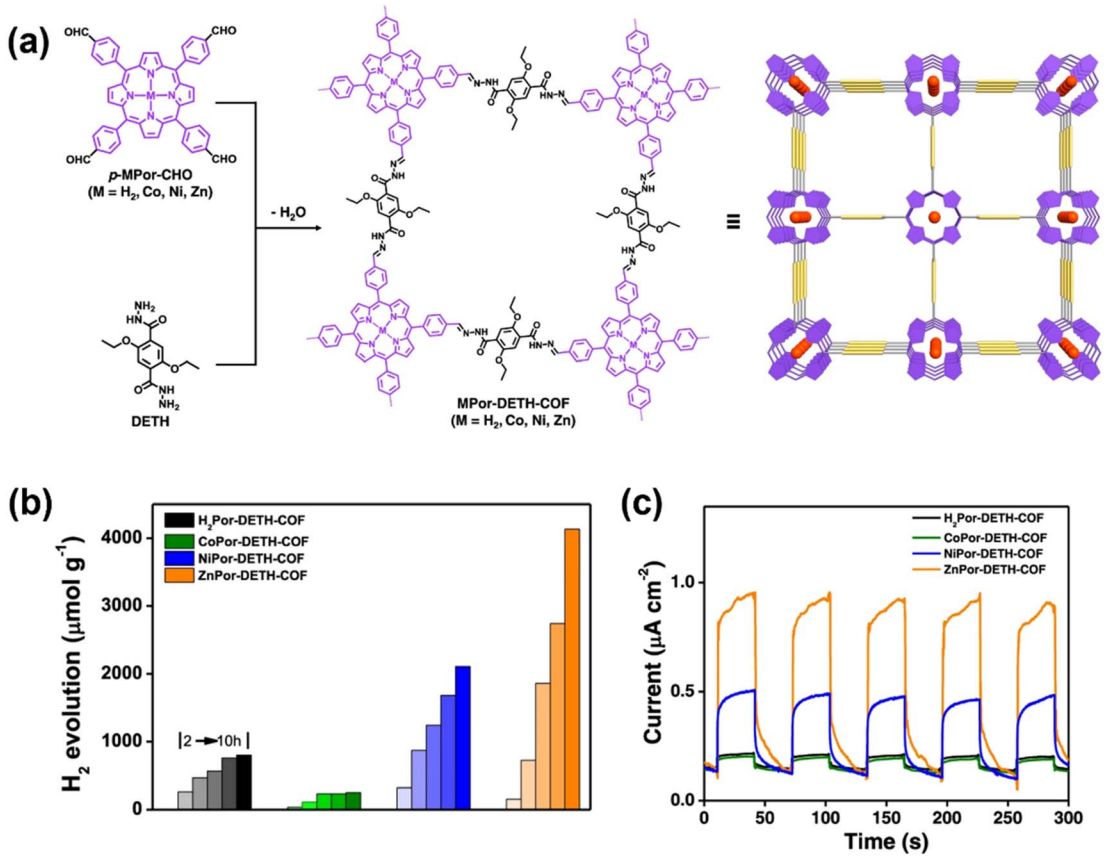

Fig. 4 (a) The construction of MPor-DETH-COFs. (b) PHE performance for MPor-DETH-COFs. (c) Photocurrent generation of all four COFs coated on an indium–tin-oxide electrode as a working electrode in a three electrode CV setup upon light on–off switching. Adapted with permission.[64] Copyright 2021, Springer Nature.

COFs different from other organic semiconductors is that they are crystalline so that their structures are well-defined, making them ideal candidates for investigation of the structure–property relationship. A series of azine-linked N_x-COFs have been synthesized with different N_x ($x = 0$, 1, 2 and 3) building units.[63] The planarity of the COFs was improved with the increasing number of N atoms in the building units and the N_3 triazine unit gave a planar 2D stacking layer. The photocatalytic activities of N_x-COFs also increased with the increasing N content and N_3-COF exhibited the highest PHE rate of 1.703 mmol h^{-1} g^{-1}. N_3-COF with a planar skeleton and extended π-conjugation offers a high BET surface area and promotes charge migration and separation. More importantly, the electron-deficient triazine unit can stabilize the negative charges and promote charge transfer to the Pt reaction center. A series of isostructural porphyrinic 2D COFs (MPor-DETH-COF, M = H_2, Co, Ni, Zn) were synthesized through the condensation reaction of porphyrinic aldehydes (p-MPor-CHO) and 2,5-diethoxyterephthalohydrazide (DETH) (Fig. 4a).[64] After incorporation of different transition metals into the porphyrin rings, the PHE performance was found to follow the order of CoPor-DETH-COF < H_2Por-DETH-COF < NiPor-DETH-COF < ZnPor-DETH-COF due to their tailored charge-carrier dynamics *via* molecular engineering (Fig. 4b), which was further confirmed by the photocurrent responses observed in the same order (Fig. 4c).

The donor–acceptor (D–A) system has been demonstrated to be effective in promoting charge transfer and suppressing charge recombination. A 2D D–A COF was constructed with the units of electron-rich pyrene (Py) and electron-deficient thiazolo[5,4-*d*]thiazole (Tz), which exhibited a PHE rate of 2072.4 μmol h^{-1} g^{-1}.[65] Employing a multicomponent synthesis strategy, a three-component D–π–A structure can be achieved to regulate the photophysical properties of COFs in a more convenient way. The Liu group reported two photoactive 2D COFs with D–π–A structures, in which a three-component donor–π–acceptor COF (TCDA-COF) was constructed from electron-deficient triazine and electron-rich benzotrithiophene units through an sp^2 carbon linkage.[66] These COFs exhibited a very high PHE rate of 70.8 ± 1.9 mmol h^{-1} g^{-1} under visible light irradiation (420–780 nm) with Pt as the co-catalyst.

A fully designable skeleton of COFs makes it very convenient to integrate various functional groups for improved photocatalytic performance. For example, a series of ketoenamine-based COFs, named TpPa-COF-X (X = –H, –$(CH_3)_2$ and –NO_2), with the same framework were selected as the model system to study the influence of different functional groups on photocatalytic hydrogen evolution (Fig. 5a).[67] The obtained TpPa-COF-$(CH_3)_2$ with an electron-donating functional group showed the best photocatalytic performance and good stability (Fig. 5b and c), while TpPa-COF-NO_2 with an electron-withdrawing

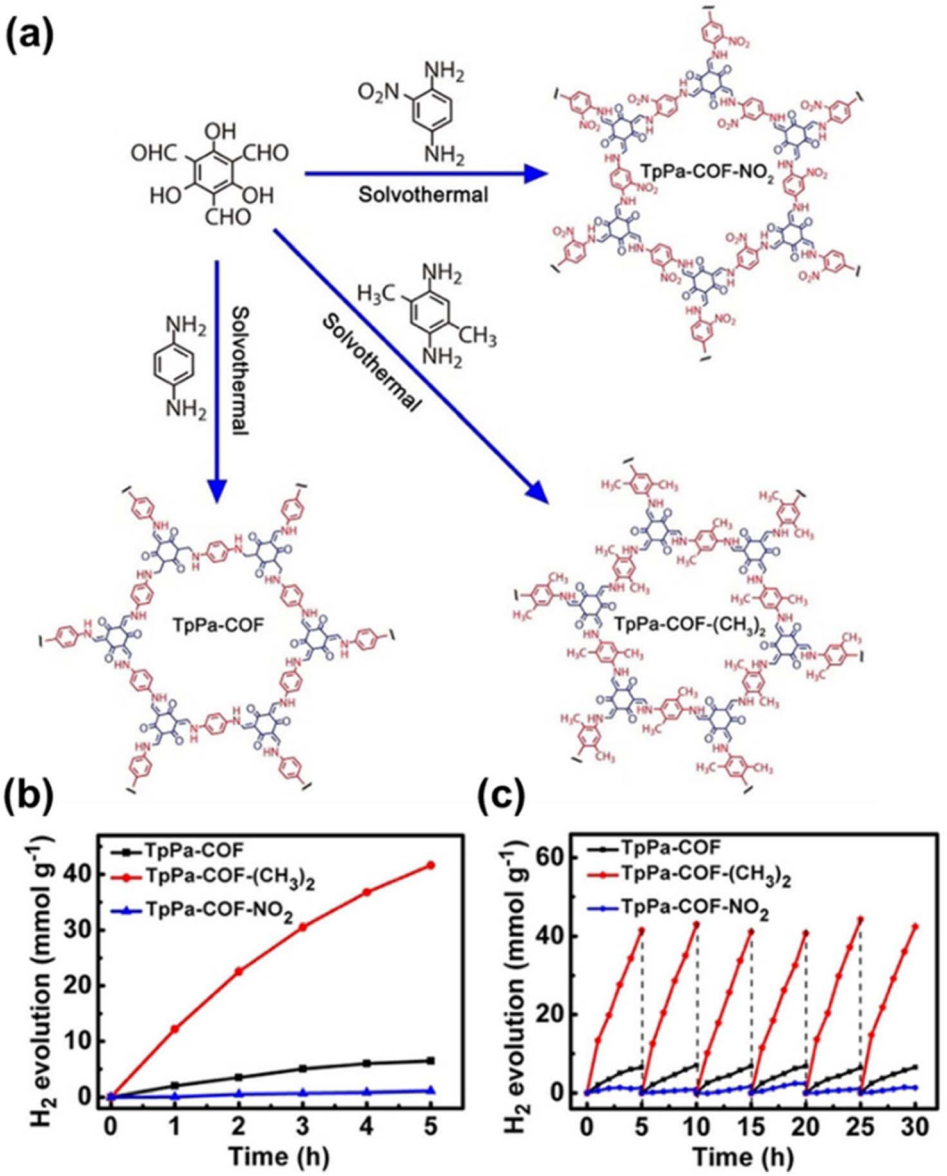

Fig. 5 (a) Schematic representation of preparation of TpPa-COF-X. (b) PHE activities and (c) photocatalytic stability of TpPa-COF-X. Reprinted with permission.[67] Copyright 2019, Wiley-VCH.

functional group exhibited the lowest PHE rate. 3-Ethylrhodanine (ERDN), as an electron deficient functional unit, has been integrated as an end-capping group in the synthetic process of sp^2c-COF and produced ERDN-terminated sp^2c-COF_{ERDN}.[68] Because of the push-and-pull effect arising from the ERDN terminating functional group, the PHE rate increased from 1360 μmol h^{-1} g^{-1} of sp^2c-COF to 2120 μmol h^{-1} g^{-1} of sp^2c-COF_{ERDN}. PY-DHBD-COF with adjacent hydroxyl groups and imine-N throughout the framework allows photogenerated electrons to converge and reduce the adsorbed platinum species into metal clusters, in which uniformly dispersed platinum clusters facilitated electron transfer, resulting in a high PHE rate of 42 432 μmol h^{-1} g^{-1} at 1 wt% Pt loading.[69]

The linkage of COFs is vital for the stability of the materials and affects the photocatalytic performance of COF photocatalysts. Three COFs adopting triphenylbenzene knots and phenyl linkers with different linkages were constructed for PHE.[70] Compared to imine- and imide-linked COFs with a low PHE rate of less than 40 μmol h^{-1} g^{-1}, the cyano-substituted alkene-linked COF showed a relatively high PHE rate of 2.33 mmol h^{-1} g^{-1} under the irradiation of visible light. Between two isomeric benzobisoxazole-bridged v-2D-COFs with *trans* and *cis* configurations of benzobisoxazole, v-2D-COF-NO1 with the *trans* configuration linkage exhibited a PHE rate of ~1.97 mmol h^{-1} g^{-1}, which is twice that of v-2D-COF-NO_2 with the *cis* configuration linkage.[71] Recent investigations by Zhang *et al.* revealed that sp^2-carbon-conjugated COFs (sp^2c-COF-ST) constructed through vinylene linkages exhibit reduced effective mass and exciton binding energy, facilitating exciton dissociation and charge separation, thereby enhancing

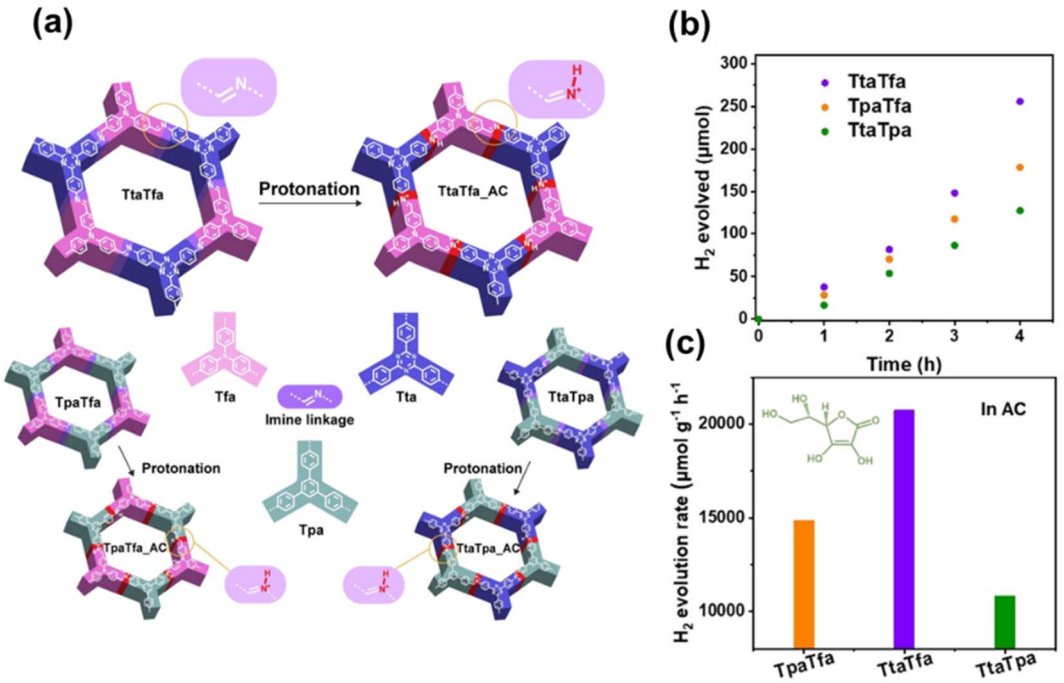

Fig. 6 (a) Synthesis of TtaTfa, TtaTfa AC, TpaTfa, TpaTfa AC, TtaTpa, and TtaTpa AC. AC = ascorbic acid modification. (b) Time course of photocatalytic H_2 evolution for TtaTfa, TpaTfa, and TtaTpa using AC as the sacrificial electron donor (SED) (3 mg catalyst, 16 mL 0.1 M AC aqueous solution, 3 μL H_2PtCl_6 (8 wt%), $\lambda > 420$ nm, and 20 °C). (c) Comparison of the photocatalytic HER rates of the above COFs using AC as the SED. Adapted with permission.[74] Copyright 2021, Wiley-VCH.

photocatalytic hydrogen evolution performance.[72] Subsequently, Xu *et al.* synthesized a cyanovinylene-linked sp^2c-Py-BT COF and imine-linked imine-Py-BT COF, both featuring identical donor–acceptor structures.[73] Benefiting from significantly lower exciton binding energy and superior stability conferred by the cyanovinylene linkage, the sp^2c-Py-BT COF demonstrated remarkable activity for photocatalytic overall water splitting, achieving an apparent quantum efficiency of 2.53% at 420 nm. In contrast, the imine-Py-BT COF failed to achieve photocatalytic water splitting. The imine linkage has been widely used for the construction of 2D COFs. When the Schiff-base linkage of a D–A COF constructed with triazine and triphenylamine motifs was protonated using ascorbic acid, a PHE rate as high as 20.7 mmol h^{-1} g^{-1} was achieved under visible light irradiation.[74] The protonated COF showed redshift in the absorption spectrum, improved charge separation and increased hydrophilicity, which are responsible for the dramatically improved photocatalytic performance (Fig. 6). Significant efforts have also been made to understand how protonation enhances the photocatalytic performance of COFs. Protonated COFs were initially employed for applications in sensing.[92] In addition to the advantages of improved hydrophilicity and broadened optical absorption range,[74] protonation can reverse the direction of charge transfer between different moieties within COFs,[93] indicating the potential for synergistic integration with other structural features.[94] Li *et al.* employed highly photoactive oligo(phenylenevinylene) building blocks in the synthesis of imine-linked COFs and implemented the protonation strategy to further enhance the photocatalytic performance. The prepared COF-954 showed an exceptionally high PHE rate of 137.23 mmol h^{-1} g^{-1}.[75] Zhang *et al.* recently reported two partially protonated COFs with significantly improved photocatalytic efficiency, which was attributed to the formation of homojunctions between pristine and protonated COFs.[95] The unique unprotonated/protonated structure generates a strong built-in electric field that effectively facilitates charge separation.

Exfoliation of 2D COFs into nanosheets (NSs) is another promising method to enhance catalytic efficiency as the layer thickness greatly affects the charge separation efficiency of COFs. CYANO-CON NSs were obtained by ball milling a cyano-containing COF (CYANO-COF) under sonication.[76] Their atomic force microscopy (AFM) images displayed irregular nanosheet topography with thickness ranging from 4 to 5 nm, corresponding to ~12–15 COF layers. The CYANO-CON nanosheets showed an impressive apparent quantum efficiency (AQY) of up to 82.6% at 450 nm. Employing a noncovalent functionalization strategy, exfoliation of the bulk crystalline covalent triazine framework (CTF) was greatly facilitated by adding 1-pyrenebutyrate (PB) in water on a large scale.[77] PB-modified 2D-TP (2D-TP-PB) was prepared by ball milling homogeneously mixed PB aqueous solution and the bulk CTF. Compared to the as-synthesized CTF, 2D-TP-PB nanosheets demonstrated an optimized band structure, a much higher PHE rate of 24.98 mmol h^{-1} g^{-1} and an AQY of up to 27.2% at 420 nm.

Morphological functionalization of COFs has also been utilized to improve their PHE performance. Wei *et al.*

synthesized unsubstituted olefin linked COFs *via* Knoevenagel condensation and named them g-$C_{18}N_3$-COF.[78] It can be organized into microfibrillar structures, facilitating the creation of additive-free, micrometer-thick thin films. The films achieve an AQY of approximately 1.06% at 420 nm, producing H_2 at a rate of 14.6 μmol h^{-1} per 50 mg of COF. The superior photocatalytic performance observed in this thin-film COF can be attributed to several intrinsic advantages of thin-film configurations. COF thin films can efficiently extract and transport charge, reducing electron–hole recombination compared to bulk powders. Their controlled thickness and large surface-to-volume ratio enhance light harvesting and mass transfer, boosting catalytic reaction kinetics. They also offer mechanical strength, easy recovery, and simple device integration.

3.1.2 Post-modified COFs with metals. The structural diversity and rich synthesis methods of COFs have brought about a variety of pathways for constructing metal–COF heterojunctions. Anchoring metals onto the frameworks with predesigned sites provides COFs with improved photocatalytic hydrogen evolution efficiency. A 2D salphen based COF was designed with double vacancies to provide sufficient coordination sites.[79] The metalized Cu-salphen-HDCOF-NSs were prepared by placing the synthesized salphen-HDCOF into methanol solution containing $Cu(OAc)_2$ for metalation and was subsequently further exfoliated into ultrathin nanosheets by facile solvent-assisted liquid sonication. The obtained Cu-salphen-HDCOF-NSs exhibited a PHE rate of 36.99 mmol h^{-1} g^{-1}, which is much higher than that of salphen-HDCOF-NSs without Cu (~4.50 mmol h^{-1} g^{-1}). As COFs themselves lack surface-active sites for the hydrogen evolution reaction, most COFs use precious metals such as Pt as co-catalysts. The development of non-noble metal co-catalysts is in high demand. Wang *et al.* have ingeniously employed hollow Co_9S_8 as a co-catalyst and grown a layer of TP-CPA-COF outside.[80] The double-shell structure enhances light absorption efficiency and reduces charge transport distances. The PHE rate of Co_9S_8@-COF is twice that using Pt as the co-catalyst. Implanting metals into the frameworks can also tune the electronic structure of COFs to optimize the photocatalytic performance. A series of hollow COF cages have been synthesized and their electronic structures were adjusted through a Zn/Co ion-implantation pathway.[81] For example, one hollow covalent organic framework cage was prepared by using ZIF-8 as a sacrificial template and condensation of 1,3,5-triformylphloroglucinol (Tp) and *p*-phenylenediamine (Pa) as the shell. ZIF-8 was then etched with acetic acid to obtain Zn@H-TpPa with Zn ions in the shell. Zn@H-TpPa showed a PHE rate of 28.0 mmol h^{-1} g^{-1}, far superior to that of pure TpPa. The incorporation of Zn within the COF gave rise to increased polarity of the framework and an upshifted conduction band of the COF, resulting in improved charge separation efficiency. Li *et al.* demonstrated an innovative *in situ* approach to construct single-atom electronic bridges (SAEBs) within metal-COFs (Fig. 7).[82] The COF was constructed using a Cu-based precursor and nitrogen-rich ligands. Upon addition of $[Ru(bpy)_3]Cl_2$ as a photosensitizer, spontaneous Ru anchoring occurred during the photocatalytic process to form interlayer Ru-SAEB structures. This design ensured an

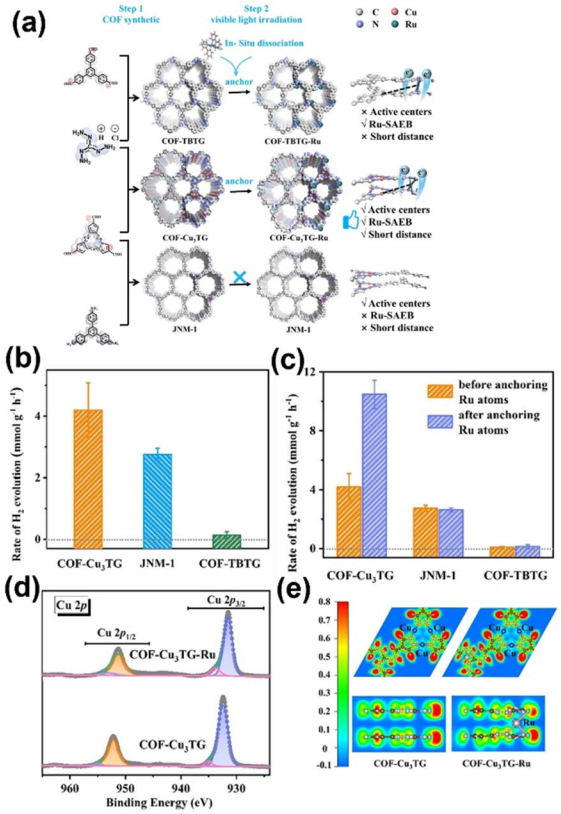

Fig. 7 (a) Synthesis and structure diagram of COF-Cu_3TG, COF-TBTG and JNM-1 (b) The rate of H_2 formation of COF-Cu_3TG, COF-TBTG and JNM-1 under visible light. (c) Rate of H_2 evolution before and after anchoring Ru atoms. (d) XPS spectra for Cu 2p. (e) ELF maps of COF-Cu_3TG and COF-Cu_3TG-Ru. Reprinted with permission.[82] Copyright 2024, Wiley-VCH.

increased density of active sites while simultaneously enabling rapid electron transport from Ru-SAEB to reaction sites, resulting in an impressive PHE rate of 10.47 mmol h^{-1} g^{-1}. XPS results confirmed the formation of a built-in electric field between Ru and Cu. The observed decrease in Cu binding energy indicates charge transfer from Ru to Cu (Fig. 7d). Electron localization function (ELF) maps revealed electron delocalization around the Ru atom in the vertical direction, further confirming the role of Ru-SAEB in facilitating electron transfer (Fig. 7e).

3.1.3 COF-based composites. Most COFs suffer from fast recombination of photo-induced electron–hole pairs. To overcome this limit, one useful strategy is to construct COF-based composites with other semiconductors to facilitate spatial separation of charges. Traditional inorganic semiconductors such as metal oxides and sulfides are good candidates to form composites with COFs. The Zhang group reported the first combination of TiO_2 and TpPa-1-COF through covalent bonds.[83] In their approach, TiO_2 was first modified with APTES and then with Tp to form CHO-TiO_2. Subsequently, the aldehyde-functionalized TiO_2 condensed with Pa to produce the TiO_2–TpPa-1-COF composite. TiO_2–TpPa-1-COF (1 : 3) with a weight ratio of 1 : 3 showed a PHE rate of 11.19 mmol h^{-1} g^{-1}, which is

5.3, 4.6 and 3.0 times higher than those of TpPa-1-COF, the TiO_2/TpPa-1-COF physiosorbed system and their composite without covalent bonds, respectively. A core–shell COF-metal sulfide composite was fabricated by self-polymerization of 1,3,5-benzenetricarboxaldehyde and 2,4,6-tris(4-aminophenyl)-1,3,5-triazine *in situ* on CdS.[84] The T-COF@CdS composites possess well-defined architectures, large contact areas and intimate contact interfaces. T-COF@CdS-3 with a mass ratio of 5 : 3 (T-COF/CdS) showed the highest PHE rate with an AQY value of 37.8% at 365 nm. Azide-functionalized molecular chloro(pyridine)cobaloxime has been immobilized onto the COF-42 backbone to form a hybrid material, which showed improved and prolonged photocatalytic activity compared to their equivalent physical mixture.[85] In this composite, molecular cobaloximes were tethered onto the backbone of propargyl-functionalized COF-42 to replace Pt nanoparticles (NPs) as the cocatalyst for the PHE reaction.

As a similar crystalline material to COFs, MOFs can be easily modified to prepare MOF/COF composites. The Lan group reported a hybrid of NH_2-UiO-66 and TpPa-1-COF for PHE.[86] NH_2-UiO-66 with an exposed $-NH_2$ group was first prepared and added to the reaction system containing Tp and Pa for the synthesis of the NH_2-UiO-66/TpPa-1-COF composite. The composite with a weight ratio of 4 : 6 for NH_2-UiO-66 : TpPa-1-COF exhibited the best PHE rate of 23.41 mmol h^{-1} g^{-1}, which is a 20-fold improvement over the pristine TpPa-1-COF. Using a similar strategy, NH_2–$Ti_3C_2T_x$ MXene was synthesized by adding Ti_3AlC_2, $Ti_3C_2T_x$ and MXene with exposed $-NH_2$ into a Pyrex tube with 4,6-trihydroxybenzene-1,3,5-tricarbaldehyde (THTA) and benzene-1,4-diamine (BDA).[87] The composite ATNT-4 with a mass ratio of 8 : 4 for NTU–BDA–THTA/NH_2–$Ti_3C_2T_x$ achieved a PHE rate of 14 228.1 μmol h^{-1} g^{-1}, which is about 12.6 times higher than that of the pure NTU–BDA–THTA COF.

Graphitic carbon nitride (g-C_3N_4) is a type of organic semiconductor with good PHE ability, a simple preparation process, cost-effectiveness, and excellent stability. However, its large band gap limits the utilization of visible light. The hybrid of g-C_3N_4 and a COF is promising to broaden the light absorption range and facilitate charge separation. A donor–acceptor type COF was used to construct TBTA/g-C_3N_4 hybrids by *in situ* condensation of 2,4,6-triformylphloroglucinol (TP) and 4,4′-(benzo-1,2,5-thiadiazole-4,7-diyl)dianiline (BTDA) on g-C_3N_4.[88] The obtained composite showed a PHE rate of 11.73 mmol h^{-1} g^{-1} without noble metals as the co-catalyst, which can be further increased to 26.04 mmol h^{-1} g^{-1} with Pt as the cocatalyst.

Assembled layers in 2D COFs are not stable under some circumstances for long-term photocatalytic applications in water. The disordered stacking will cause decreased photocatalytic activity. To solve this problem, polyethylene glycol (PEG) was utilized to fill up the mesopore channels of a benzothiadiazole-based COF linked by β-ketoenamine linkages (Fig. 8a).[89] This unique procedure prevents the neighboring layers from disordering and retains the columnar π-orbital arrays to facilitate photo-induced charge transport. A significantly improved PHE rate was achieved compared to that of the pristine COF under visible light irradiation (Fig. 8b).

Heterojunctions were generally constructed through covalent bonding and *in situ* growth strategies to ensure tight interfacial contact. Li *et al.* demonstrated an effective approach to constructing Z-scheme heterojunctions by integrating photosensitive metal–organic rings (MAC-FA1) with coral-like S-COF through supramolecular interactions. Compared with covalent binding strategies, this supramolecular approach offers greater synthetic flexibility for combining diverse metal–organic rings with semiconductor materials. In this system, photosensitive MAC-FA1 served as the catalytic site, while S-COF functioned as an efficient light harvesting complex. The optimized 4% MAC-FA1/S-COF heterojunction exhibited remarkable photocatalytic performance with a PHE rate of 100 mmol h^{-1} g^{-1} without additional cocatalysts, representing a significant advancement over conventional COF-based composites.[90] Luan *et al.* demonstrated a COF/COF Z-scheme heterojunction by integrating two different COFs through π–π interactions between conjugated aromatic rings. The optimized COF-316/Pt@TpBpy-COF heterojunction with a weight ratio of COF-316 : TpBpy-COF = 2 : 8 exhibited remarkable overall water splitting performance with H_2 and O_2 evolution rates reaching 220.4 and 110.2 μmol h^{-1} g^{-1} respectively under visible light.[91]

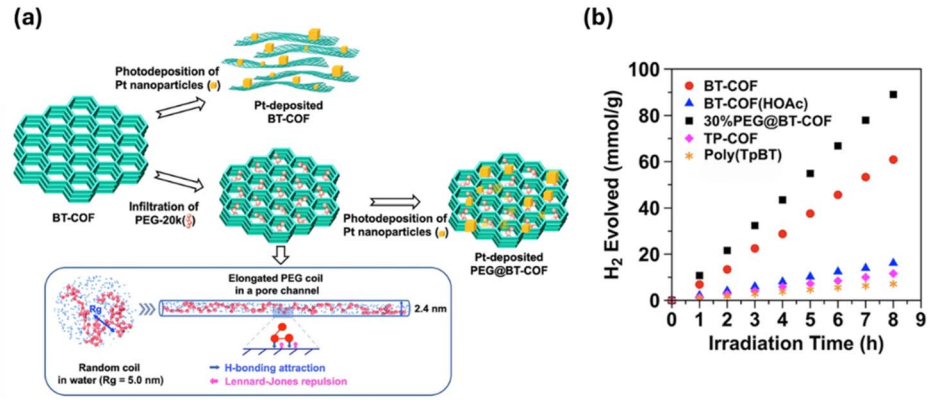

Fig. 8 Illustration of structural transformation of BT-COF and PEG@COF during the deposition of Pt. Reprinted with permission.[89] Copyright 2021, Springer Nature.

These studies demonstrate that constructing organic heterojunctions through non-covalent interactions offers an effective strategy to achieve efficient charge separation and transfer for photocatalytic applications.

3.2 Photocatalytic CO_2 reduction

Carbon dioxide (CO_2) is an environmentally harmful greenhouse gas and a potential carbon resource as well. Photoreduction of CO_2 to value-added chemical fuels can not only solve the environmental problem but also provide a new way to develop carbon resources. However, it is very difficult to activate the rigid C=O bond in carbon dioxide as the reduction of CO_2 involves multiple electrons, which is more complex than water splitting. COFs combine tunable energy diagrams, light-harvesting capability, and catalytic activity at the same time and therefore can act as great candidates for photocatalytic CO_2 reduction.[96] Table 2 summarizes the photocatalytic CO_2 reduction performance of different COF-based photocatalysts.

3.2.1 Pristine COFs. In 2018, two 2D azine-based COFs were synthesized by condensing 1,3,5-triformylbenzene (TFB) and 2,4,6-tris(4-bromophenyl)-1,3,5-triazine (N_3-Ald) with hydrazine hydrate, respectively.[97] These were the first metal-free azine-based COFs that achieved CO_2 reduction to methanol under visible light irradiation without any sacrificial agent. This work reveals the great potential of COFs for photocatalytic CO_2 reduction owing to their structural diversity and tunability. Precise COF design at the molecular level provides structural flexibility, which can profoundly affect their photocatalytic performance. Streater *et al.* conducted a systematic investigation of imine bond directionality in COFs and observed that the forward imine COF achieved effective CO_2 reduction while the reversed imine COF showed minimal activity, highlighting the significant influence of subtle structural changes on their photocatalytic performance.[98] By using acid-catalyzed Schiff-base condensation of 2,6-diaminobenzo[1,2-*d*:4,5-*d*′]bisthiazole (Bb-NH_2) and 1,3,5-triformylphloroglucinol (Tp-CHO) in mesitylene/dioxane, Liu *et al.* synthesized a metal-free β-ketoenamine-based COF, named TpBb-COF.[99] Without using additional photosensitizers and sacrificial agents, TpBb-COF showed a photocatalytic carbon monoxide (CO) production

Table 2 Summary of CO_2 reduction performance of COF-based photocatalysts

Samples	Irradiation conditions	CO_2 reduction products (μmol h^{-1} g^{-1})	Selectivity	Ref.
N_3-COF	800 nm ≥ λ ≥ 420 nm	CH_3OH (0.57)	—	97
Re-f-COF	λ > 420 nm	CO (787.5)	—	98
TpBb-COF	λ ≥ 420 nm	CO (89.9)	—	99
QL-COF	AM 1.5	CO (156)	99.3%	100
TAPBB-COF	1000 nm ≥ λ ≥ 200 nm	CO (24.6)	95.6%	101
HCOF-2	λ > 420 nm	CO/CH_4 (30.9/9.6)	—	102
COF-367-Co^{III}	λ > 380 nm	HCOOH (93)	97.1%	103
JUC-640-Co	λ > 380 nm	CO (15 100)	94.4%	104
Cu_4COF-2	Full spectrum	CO (23.8)	94.3%	105
EPCo-COF-AT	λ ≥ 420 nm	CO (17 700)	97.8%	106
Re-Bpy-sp_2c-COF	λ > 420 nm	CO (1040)	81%	107
Ni-TpBpy	λ ≥ 420 nm	CO (811.4)	96%	108
Fe SAS/Tr-COF	λ > 420 nm	CO (980.3)	96.4%	109
DQTP COF-Co	λ ≥ 420 nm	CO (1020)	—	110
Co-COF	λ ≥ 420 nm	CO (18 000)	95.7%	111
H-COF-Ni	λ ≥ 420 nm	CO (2847)	96%	112
Ni-TP-CON	λ ≥ 420 nm	CO (4360)	95%	113
Co/Cu_3-TPA-COF	λ ≥ 420 nm	CO (25 247.7)	80.2	114
CoNi-COF-3	λ ≥ 420 nm	CO (2567)	92.2%	115
Ru/TpPa-1	800 nm ≥ λ ≥ 420 nm	HCOOH (108.8)	—	116
Ru@TpBpy	800 nm ≥ λ ≥ 420 nm	HCOOH (172)	—	117
Co_x-COF	λ ≥ 420 nm	CO (4232)	—	118
TCOF-$MnMo_6$	800 nm ≥ λ ≥ 400 nm	CO (37.25)	100%	119
BBO-COF_{BPY}-Co	Full spectrum	CO (10 552.15)	91%	120
COF-318-TiO_2	800 nm ≥ λ ≥ 380 nm	CO (69.97)	—	121
TiO_2-INA@CuP-Ph COF	AM 1.5	CO (50.5)	—	122
NCTS	Full spectrum	CO (7.51)	100%	123
T-101/COF	Full spectrum	CO (11.6)	95%	124
CdS@COF	λ ≥ 420 nm	CO (507)	72%	125
CdS/TpBpy	Full spectrum	CO (5028)	85%	126
g-C_3N_4 (NH)/COF	λ > 400 nm	CO (562.5)	—	127
TpPa/ZIF-8	LED	CO (84.87)	> 90%	129
TMBen-perylene	λ > 420 nm	CO (93)	96%	130
NKCOF-113	λ > 420 nm	HCOOH (360)	—	131
GO-COF-366-Co	λ > 320 nm	Formate (19 750)	94.4%	132
		CO (6525)	96.1%	
COF@TI	800 nm ≥ λ ≥ 400 nm	CO/H_2 (470/237)	—	133

rate of 89.9 μmol h^{-1} g^{-1} under a CO_2 concentration of 30%. Experimental and theoretical calculation results suggest that the cyclohexanetrione moiety of TpBb-COF preferentially adsorbs H_2O *via* hydrogen bonding, which enhances the adsorption of CO_2 and promotes the conversion from CO_2 to CO. The work by Jin *et al.* further supports the strategy of constructing COFs with a hydrophilic structure to enhance the photocatalytic CO_2 reduction efficiency.[100] QL-COF and LZU1-COF were synthesized from the same precursors 1,3,5-triformylbenzene and 1,4-diaminobenzene. QL-COF was constructed using a hydrophilic 4-carboxyl-quinoline linkage, while LZU1-COF was built *via* an imine linkage. The photocatalytic CO production performance of QL-COF was >6 times that of LZU1-COF. The higher performance of QL-COF was attributed to the presence of hydrophilic –COOH groups that strongly bind with H_2O molecules to further improve the adsorption of CO_2 molecules.

The highly flexible structure of COFs makes it easy to decorate functional groups to tune their properties and thus improve photocatalytic performance. COF-366 exhibited high carrier mobility and efficient visible light absorption,[134] while its photocatalytic CO production rate was only 8.5 μmol h^{-1} g^{-1} in a gas–solid phase reaction under full-spectrum light irradiation.[101] Su *et al.* found that the oxidation reaction was hindered by the negligible difference (0.04 V) between the valence band of COF-366 (VB; +0.86 V) and the redox potential of O_2/H_2O (+0.82 V).[101] A halogenation strategy was proposed to functionalize COF-366 with bromine groups to synthesize a novel COF, namely TAPBB-COF. With a more positive VB value (+1.10 V) than that of COF-366, TAPBB-COF facilitated the oxidation half reaction more effectively. Consequently, TAPBB-COF produced CO at a rate of 24.6 μmol h^{-1} g^{-1}, which was approximately three-fold higher than that of COF-366 under identical conditions. Jiang *et al.* prepared three distinct COFs (HCOF-1, HCOF-2 and HCOF-3) by using hydrazine hydrate (HZ) with three different aldehyde precursors, 1,3,5-triformylphenol, 1,3,5-triformylresorcinol, and 1,3,5-triformylphloroglucinol.[102] Due to different proportions of hydroxyl groups in the skeleton, HCOF-1 did not exhibit keto–enol tautomerism, while HCOF-2 showed reversible keto–enol tautomerism and HCOF-3 displayed irreversible keto–enol tautomerization. Based on the experimental and density functional theory (DFT) calculation results, reversible keto–enol tautomerism led to an extended light-harvesting range and enhanced charge separation and transportation. Consequently, HCOF-2 showed the highest photocatalytic performance, producing CO and CH_4 with a rate of 30.9 and 9.6 μmol h^{-1} g^{-1}, respectively.

Porphyrin-based COFs with 18 electron π-conjugated macrocycles are promising in photocatalysis due to their efficient visible light absorption and easy incorporation of various metal ions as active sites. Jiang *et al.* devised a simple strategy to manipulate the cobalt spin state in COF-367-Co by altering the oxidation state of Co in the porphyrin center.[103] DFT calculation and experimental results suggest that Co^{II} and Co^{III} with spin ground states of $S = 1/2$ and 0 were incorporated into COF-367. Photocatalytic CO_2 reduction results reveal that COF-367-Co^{III} exhibited better activity and remarkably improved selectivity to HCOOH compared with COF-367-Co^{II}. Recently, Fang *et al.* synthesized a series of 3D **stp**-topologized porphyrin COFs (JUC-640-M, M = H, Co, or Ni) by polymerizing the 6-connected triptycene-based building unit, 2,3,6,7,14,15-hexa(4′-formylphenyl)triptycene (HFPTP, D_{3h}-symmetrized), with 4-connected 5,10,15,20-tetrakis(4-aminophenyl)porphyrin (TAPP-H, D_{4h}-symmetrized) or its metallized derivatives (TAPP-Co and TAPP-Ni), as shown in Fig. 9a.[104] Extraordinarily, JUC-640-H has the lowest crystal density (0.106 cm^3 g^{-1}) ever reported for any crystalline material and the largest interconnected channels (4.6 nm) among 3D COFs. These features, along with a high surface area (2204 m^2 g^{-1}), large and interpenetrated channels and abundant exposed porphyrin moieties (0.845 mmol g^{-1}), made these 3D COFs efficient photocatalysts for CO_2 reduction under visible light irradiation. The photocatalytic CO production rate of JUC-640-Co reached as high as 15.1 mmol h^{-1} g^{-1}, with a high selectivity (94.4%) and stability (Fig. 9b and c). Similarly, the metal phthalocyanines with 18π aromatic macrocyclic structures represent ideal building blocks for COFs, which exhibit exceptional photosensitivity and abundant single-atom sites. Xu *et al.* prepared highly stable and reactive copper cluster-based COFs (Cu_4COF-1 and Cu_4COF-2) *via* a stepwise assembly approach involving epitaxially amino-modified Cu_4 clusters (Cu_4–NH_2), as shown in Fig. 9d–f.[105] These Cu_4COFs exhibited enhanced stability, narrower band gaps, larger specific surface areas, and superior charge transfer capabilities compared to isolated Cu_4 clusters, leading to significantly

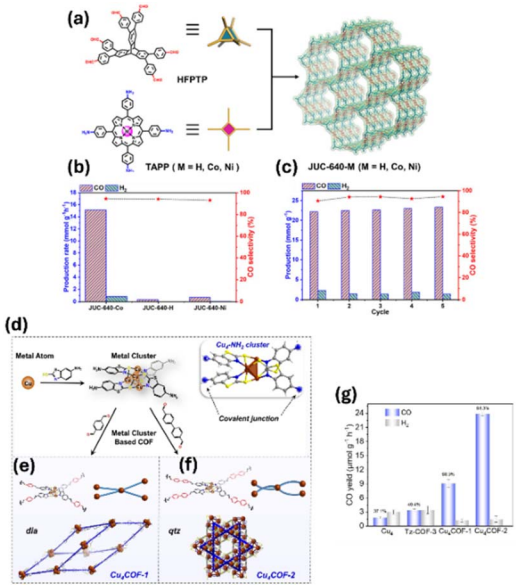

Fig. 9 (a) Schematic illustration of the construction of JUC-640-M (M = Co, Ni, or H). (b) Comparison of the photocatalytic activity of JUC-640-M. (c) Stability tests of JUC-640-Co (2 h each cycle). Reprinted with permission.[104] Copyright 2023, American Chemical Society. (d) The illustration of step-by-step precise assembly procedures of Cu_4 cluster-based COFs; inset: single crystal structure of Cu_4. The structural representation of (e) Cu_4COF-1 with dia topology and (f) Cu_4COF-2 with qtz topology. (g) Photocatalytic CO_2-to-CO performance and selectivity of Cu_4, Tz-COF-3, Cu_4COF-1 and Cu_4COF-2. Reprinted with permission. Copyright 2025, Wiley-VCH.

improved photocatalytic CO_2 reduction performance under visible light. Specifically, Cu_4COF-2 achieved a CO production rate of 23.8 μmol g^{-1} h^{-1} with an impressive selectivity of 94.3% (Fig. 9g). Wang *et al.* synthesized a novel class of COFs, designated as EPM-COF (M = Co, Ni, Cu), by integrating perfluorinated metallophthalocyanine with ellagic acid. Notably, following alkaline treatment, EPCo-COF demonstrated remarkable photoactivity in CO generation with a production rate of 17.7 mmol h^{-1} g^{-1}.[106]

COFs of different morphologies with certain functions have also been prepared to further improve the photocatalytic CO_2 reduction performance. Cooper *et al.* developed fibrous COFs, which exhibit a very high CO production rate of 1.04 mmol h^{-1} g^{-1} and a selectivity of 81% during light exposure.[107] This excellent performance was primarily ascribed to the unique fiber morphology that can increase the effective light absorption through light scattering, improve the penetration depth, and enhance the photon utilization efficiency. Furthermore, the continuous fiber structure facilitates the efficient transport of photogenerated electrons and holes along a one-dimensional conductive path, greatly hindering the electron–hole recombination. Finally, its high aspect ratio provides a large number of accessible surfaces and facilitates mass transfer, significantly enhancing photocatalytic kinetics.[107]

3.2.2 Post-modified COFs with metals. The lack of exposed metal catalytic centers in most COFs leads to poor activity and selectivity in photocatalytic CO_2 reduction. Fortunately, the structural diversity of COFs offers a rich variety of well-defined metal-binding sites for post-synthetic modification. Zou *et al.* prepared a 2,2′-bipyridine-based COF (TpBpy) by the condensation of 1,3,5-triformylphloroglucinol and 5,5′-diamino-2,2′-bipyridine.[108] A single Ni site modified COF (Ni-TpBpy) was subsequently obtained by coordination of Ni^{2+} with 2,2′-bypridine units in TpBpy. Ni-TpBpy exhibited outstanding photocatalytic performance with a CO generation rate of 811.4 μmol h^{-1} g^{-1} in a 5 h reaction and a selectivity of 96% for CO over H_2. Henceforth, single Co,[135,136] Cu,[137] and Mo[138] sites were immobilized in COFs with bipyridine units and achieved efficient photocatalytic CO_2 reduction. In addition to bipyridine units, single metal sites have also been anchored to the triazine units. Hou *et al.* integrated 4,4′,4″-(1,3,5-triazine-2,4,6-triyl) trianiline and acenaphthenequinone monomers to form a triazine-based COF (Tr-COF).[109] A series of single-atom metal sites (*e.g.*, Fe, Co, Ni, Zn, Cu, Mn, and Ru) were fixed on the Tr-COF skeleton (SAS/Tr-COF) through a metal–nitrogen–chlorine bridging structure (Fig. 10a). The performance of Fe SAS/Tr-COF in photocatalytic CO_2 reduction was superior to that of other Tr-COFs with single-atom metal sites. It generated CO at a rate of 980.3 μmol h^{-1} g^{-1} and a selectivity of 96.4%, which was about 26 times higher than that of the pristine Tr-COF (Fig. 10b and c). The atomically dispersed metal sites and Tr-COF host synergistically lowered the reaction energy barrier for the formation of the *COOH intermediate, enhanced CO_2 adsorption and activation, and facilitated CO desorption, resulting in a surpassing photocatalytic activity (Fig. 10d). Fe SAS/Tr-COF exhibited a higher CO_2 adsorption capacity due to its lower energy barrier relative to that of pristine Tr-COF. These COF-Fe displayed stronger

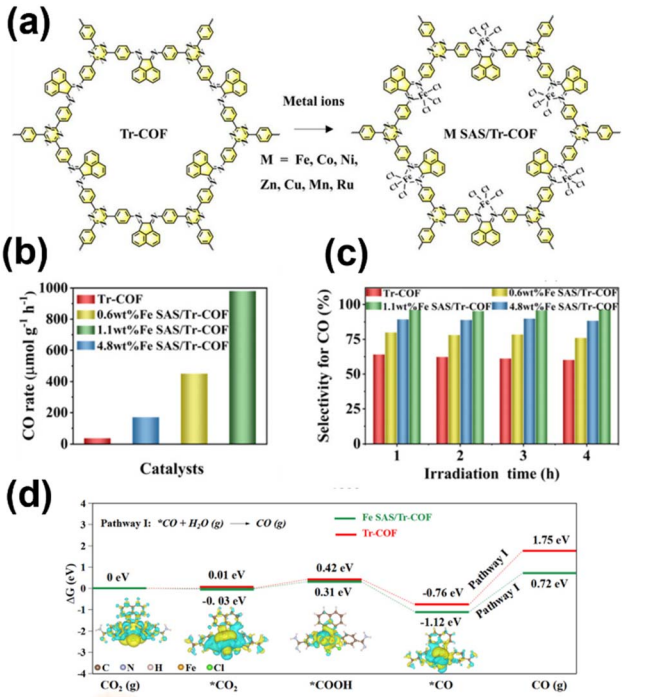

Fig. 10 (a) Synthetic of M SAS/Tr-COF. (b) CO generation rate and (c) calculated CO selectivity over Tr-COFs, 0.6 wt% Fe SAS/Tr-COFs, 1.1 wt% Fe SAS/Tr-COFs, and 4.8 wt% Fe SAS/Tr-COFs in 4 h under visible light irradiation. (d) DFT-calculated Gibbs free energy (Δ*G*, eV) profiles for CO_2 photoreduction on Fe SAS/Tr-COFs and Tr-COFs with the corresponding geometry structures and differential charge densities of intermediates over Fe SAS/Tr-COFs. Adapted with permission.[109] Copyright 2022, American Chemical Society.

affinity for CO_2 at Fe sites compared with the pristine COF. This affinity is critical for suppressing competitive reactions to enhance the selectivity of Fe SAS/Tr-COF catalysts over Tr-COF catalysts.

Single metal atoms have also been successfully immobilized onto COFs by metal–O or metal–O/N binding. By exploiting the high affinity of the anthraquinone group toward metal atoms, Lan *et al.* prepared transition metal modified DQTP (2,6-diaminoanthraquinone-2,4,6-triformylphloroglucinol) COFs (DQTP COF-M, M = Co, Ni, Zn).[110] DQTP COF-Co showed an impressive CO production rate of 1.02 × 10^3 μmol h^{-1} g^{-1}, whereas DQTP COF-Zn exhibited a high preference for the formation of HCOOH (152.5 μmol h^{-1} g^{-1}). Wang *et al.* synthesized two types of COFs with oxygen coordinated Co atoms by using 2,4,6-tris(4-aminophenyl)-1,3,5-triazine (TAPT) as a fixed module and varying aldehyde molecules, referred to as Co-2,3-DHTA-COF and Co-TP-COF, containing Co-O_4 and Co-O_3N sites, respectively (Fig. 11a).[111] Based on the experimental and DFT calculation results, the unique Co-O_4 coordination environment in Co-2,3-DHTA-COF increased the Co(II) loading amount in the COF, facilitated the charge transfer from the photosensitizer to the catalyst, improved the CO_2 adsorption capacity, and lowered the energy barrier of the rate-determining step. Co-2,3-DHTA-COF thus exhibited an outstanding photocatalytic CO production rate of 18 000 μmol h^{-1} g^{-1} and reached

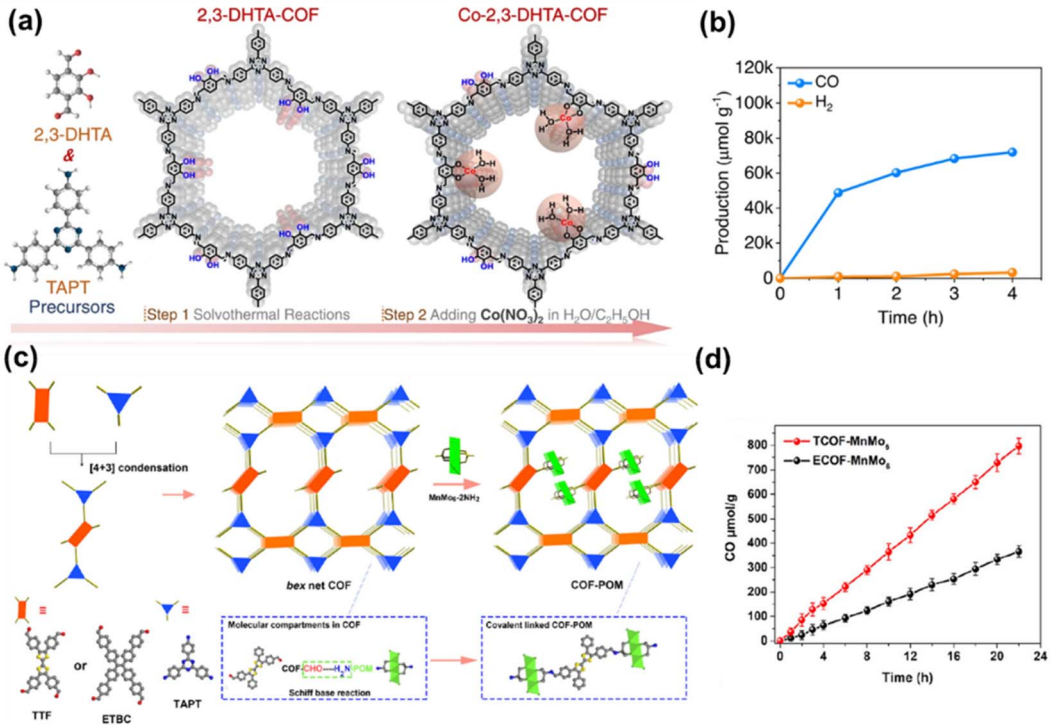

Fig. 11 (a) Synthesis of 2,3-DHTA-COF and Co-2,3-DHTA-COF. (b) CO and H_2 evolution with irradiation time for the CO_2RR catalyzed by Co-2,3-DHTA-COF under visible light irradiation. Adapted with permission.[111] Copyright 2023, Springer Nature. (c) Schematic of uniformly dispersed POM clusters in the COF by confining them into the pores of the COF through covalent linkages. (d) Time-dependent CO_2-to-CO performance for TCOF-$MnMo_6$ and ECOF-$MnMo_6$. Reproduced with permission.[119] Copyright 2022, American Chemical Society.

a high selectivity of 95.7% under visible light conditions (Fig. 11b). Moreover, Ni ions were anchored into H-COF by chelating coordination with an *N*-acylhydrazone linkage.[112] Single Cu-O/N sites were formed on the DHTA–TTA 2D COF by binding Cu with the imine and methoxy groups.[139] In another study, Ni active sites were immobilized in TP-CON *via* bis-chelating coordination.[113] All the above metallized COFs exhibited excellent photocatalytic CO_2 reduction activity. Single cobalt sites have been recently incorporated into the interlayer of COFs (Cu_3-TPA-COF, Cu_3-TAPB-COF, and Cu_3-TAPT-COF) by coordination *via* imine-N motifs. The Co-imine N moieties were integrated into donor[1]–acceptor–donor[2] architectures to give rise to the formation of a well-separated electron–hole state. This unique configuration efficaciously induces vectorial electron transfer from dual electron-donating domains to the cobalt centers, thereby facilitating CO_2 activation and subsequent reduction.[114]

The incorporation of bimetallic sites into COFs to promote photocatalytic CO_2 reduction activity by synergistic effects has attracted a lot of attention. Lin *et al.* introduced a three-step synthesis of FeNi bimetallic COFs. Pure COFs were fabricated from 2,4,6-triformylphloroglucinol and 2,5-diaminobenzenesulfonic acid and NH_4-COFs were subsequently obtained by an ammoniating process.[140] Metal ions (Fe^{3+}, Ni^{2+}, and Co^{2+}) were attached onto COFs by a cation-exchange method through strong interactions with the abundant $-SO_3^-$ units. By varying the ratio of Fe/Ni sites on the COFs, the photoreduction of low content CO_2 to syngas with a wide range of tunability was realized. In these materials, the Fe and Ni sites play distinct roles in the catalytic process: the Fe sites facilitate H_2 production by strongly binding H_2O, while the Ni sites favor CO production by preferentially adsorbing CO_2. Recently, Lan *et al.* modified three kinds of benzothiadiazole-based COFs with Co and Ni dual-metal sites by metal–thiadiazole interaction (CoNi-COF-*n*, $n = 0$, 1, 2, and 3).[115] Benefiting from the synergistic effect of the fully β-ketoenamine-tautomerized COF-3 configuration and dual-metal sites, CoNi-COF-3 showed a high CO production rate of 2567 μmol h^{-1} g^{-1} with a selectivity of 92.2%. Besides, metal NPs were decorated onto the COF matrix to accelerate CO_2 photoreduction. Fan *et al.* fixed Ru NPs onto a ketoamine-based COF (Ru/TpPa-1) and achieved a photocatalytic formic acid generation rate of 108.8 μmol h^{-1} g^{-1} with a Ru loading of 3.0 wt%.[116] The presence of Ru NPs promoted visible light harvesting, improved the charge transfer, and inhibited charge recombination. Ru NPs were also loaded onto a bipyridine-based COF (Ru@TpBpy), which produced HCOOH with a rate of 172 μmol h^{-1} g^{-1} under a low Ru loading (0.7 wt%).[117] Furthermore, Bi *et al.* immobilized Co quantum dots (QDs) onto COF-318, realizing a photocatalytic CO generation rate of 4232 μmol h^{-1} g^{-1} and a H_2 evolution rate of 6611 μmol h^{-1} g^{-1}.[118] Here, Co QDs contribute to the enhanced activity by not only serving as an electron trap to promote charge separation but also boosting the adsorption and activation of CO_2 molecules. Moreover, single POM clusters were restricted

within the nanopores of COFs. Lan *et al.* synthesized a subvalent COF, specifically TCOF, *via* a [4 + 3] Schiff-base condensation of 2,3,6,7-tetrakis(4-formylphenyl)tetrathiafulvalene (TTF-4CHO) and 2,4,6-tris(4-aminophenyl)-1,3,5-triazine (TAPT) under solvothermal conditions (Fig. 11c).[119] TCOF and POM were then covalently bonded to form TCOF-$MnMo_6$ by the Schiff-base reaction between the uncondensed aldehyde functional groups in the pores of TCOF and amine-functionalized POM ($MnMo_6$-$2NH_2$). By integrating the merits of both components, TCOF-$MnMo_6$ demonstrated high performance in yielding CO with a rate of 37.25 μmol h^{-1} g^{-1} and a selectivity of approximately 100% (Fig. 11d).

Zhang *et al.* reported three benzoxazole-based COFs with distinct cobalt coordination geometries (Co–N–O_2, Co–N–O_3, and Co–N_2–O_2). Through post-synthetic modification, precise control over the catalytic microenvironment was achieved, where Co was anchored by coordination with imine–nitrogen atoms, imine–nitrogen and adjacent hydroxyl groups, and bipyridine units, respectively. The optimized BBO-COF_{BPY}-Co catalyst demonstrated remarkable performance with a CO production rate of 10.55 mmol h^{-1} g^{-1} and a selectivity of 91%, surpassing many previous COF-based systems. Mechanism studies revealed that rational engineering of the Co coordination environment could optimize the local electronic structure of BBO-COFs, promoting efficient exciton dissociation and charge carrier migration while suppressing electron–hole recombination. This work not only achieved high catalytic activity but also provided insights into the influence of metal coordination environments on the photocatalytic CO_2 reduction process, complementing other strategies in metal-modified COF design.[120]

3.2.3 COF-based composites. Various semiconducting photocatalysts have been employed to construct Z-scheme or type II heterojunctions with COFs, such as TiO_2,[121–124] CdS,[125,126] g-C_3N_4,[127,128] and MOFs[129] for enhanced photocatalytic CO_2 reduction performance. Lan *et al.* fabricated a series of covalently bonded COF/oxide-semiconductor heterojunctions (COF-SC : COF-TiO_2, Bi_2WO_6, and α-Fe_2O_3), as shown in Fig. 12, by utilizing the interaction of abundant hydroxyl functional groups on the surface of oxide-semiconductors with strong electron-withdrawing substituents on TFPN/TFPC building blocks.[121] Among these prepared COF-SC, COF-318-TiO_2 demonstrated the maximal CO production rate of 69.67 μmol g^{-1}. *In situ* XPS spectra were utilized to confirm the Z-scheme charge transfer pathway. The positive shift in Ti 2p binding energy under UV irradiation indicated a decrease in electron density at Ti sites (Fig. 12c), confirming that photogenerated electrons migrated from TiO_2 to COF-318. As illustrated in Fig. 12d, electron transfer from TiO_2 to COF-318 *via* covalent bonds results in electron accumulation at the cyano/pyridine units of COF-318 for CO_2 reduction, while holes remain in TiO_2 to facilitate H_2O oxidation. The unsatisfactory intramolecular electron transfer in imine-linked COFs limits its photocatalytic performance. Wang *et al.* reported a CdS@COF core–shell photocatalyst, where the imine-linked COF was constructed from Zn-porphyrin and Co-bipyridyl units.[125] They found that CdS acted

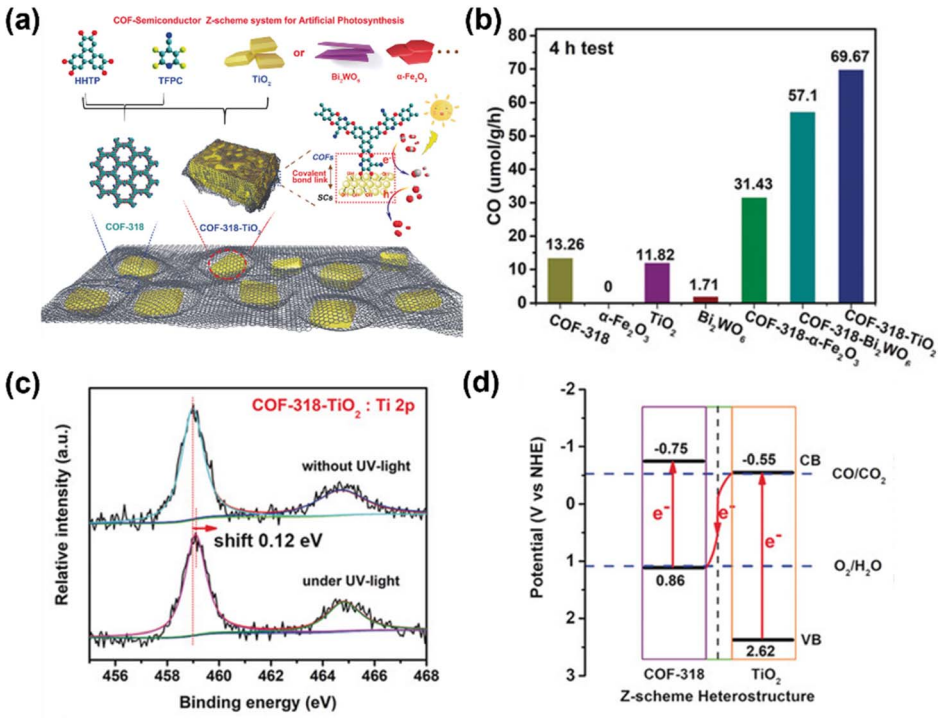

Fig. 12 (a) Schematic illustration of the preparation of COF-318-SCs. (b) Photocatalytic performance of various COF-318-SCs as well as bulk COF-318, TiO_2, Bi_2WO_6, and α-Fe_2O_3. (c) High-resolution *in situ* XPS for Ti 2p of COF-318-TiO_2 in the dark and under 365 nm LED irradiation; (d) schematic illustration of the charge-transfer process under light irradiation with the Z-scheme model. Adapted with permission.[121] Copyright 2020, Wiley-VCH.

as a channel for photo-induced electron transfer from Zn-porphyrin to Co-bipyridyl units to avoid an inefficient pathway *via* a highly polarized imine linkage. CdS@COF showed an obviously enhanced CO production rate of ~507 μmol h^{-1} g^{-1} compared with pure CdS and the pristine COF. Ye *et al.* synthesized a van der Waals heterojunction of defective g-C_3N_4 (NH)/COF with S-scheme charge transfer, exhibiting a CO evolution rate of 11.25 μmol h^{-1}, which is 45 and 15 times higher than that of g-C_3N_4 and g-C_3N_4/COF, respectively.[128] Su *et al.* constructed COF/MOF hybrids (TpPa/ZIF-8) by simply grinding a blend of TpPa-1, $Zn(OAc)_2 \cdot 2H_2O$ and 2-IM.[129] In the absence of photosensitizers and sacrificial agents, the optimized TpPa/ZIF-8 photocatalyst exhibited a CO evolution rate of 84.87 μmol h^{-1} g^{-1} when CO_2 concentration is only 10%.

In addition to traditional semiconductors, dyes and enzymes are also combined with COFs for efficient CO_2 photoreduction. Zhou *et al.* separately combined three polycyclic aromatic hydrocarbons (anthracene, pyrene and perylene) with olefin-linked COFs (TMBen) through the aldol condensation reaction.[130] TMBen–perylene establishes a type II band alignment, which significantly restrained charge recombination by accumulation of electrons and holes on TMBen and perylene domains, respectively (Fig. 13a). Consequently, TMBen–perylene showed an 8 times improvement over pristine TMBen in the photocatalytic reduction of CO_2 to CO (Fig. 13b). Chen *et al.* reported the immobilization of formate dehydrogenase in an olefin-linked COF (NKCOF-113) to build a novel photoenzymatic system for photocatalytic HCOOH production.[131] In this system, NKCOF-113 served as a photosensitizer to provide photogenerated electrons to the Rh moieties, which react with NAD^+ to form a nicotinamide cofactor (NADH). Formate dehydrogenase converted CO_2 to formic acid by employing NADH and NAD^+ was regenerated simultaneously to participate in the next photocatalysis cycle.

Besides dyes and enzymes, graphene-based materials and topological quantum materials have emerged as promising components for COF-based composites. Gong *et al.* developed a covalently anchored COF-GO composite (GO-COF-366-Co) that exhibited interesting solvent-dependent selectivity for CO_2 reduction. In acetonitrile (CH_3CN), the composite showed a high selectivity of 94.4% for formate production with a yield of 1.975 mmol h^{-1} g^{-1}, while switching to an CH_3CN/H_2O mixture (4 : 1) led to preferential CO production with 96.1% selectivity and a CO yield of 6.525 mmol h^{-1} g^{-1}. Photoelectrochemical studies and *in situ* FTIR revealed that the covalent integration created efficient charge-transfer bridges and stabilized key reaction intermediates through hydrogen bonding interactions, which facilitated efficient charge separation and transfer.[132]

Very recently Dey *et al.* demonstrated a novel approach by integrating a 2D COF with a strong topological insulator (TI), $PbBi_2Te_4$, to form a unique COF-topological quantum material nano-heterostructure. The robust metallic surface of TI served as an electron reservoir to minimize electron–hole recombination, while the presence of $6s^2$ lone pairs in Pb^{2+} and Bi^{3+} facilitated CO_2 binding. This synergistic design enabled tunable syngas production with controllable CO : H_2 ratios through adjustment of the acetonitrile/water ratio.[133]

3.3 Photocatalytic organic transformation

Light-induced organic transformations are regarded as environmentally friendly and sustainable alternatives for the synthesis of fine chemicals. Organic transformation reactions employing traditional catalysts such as metal complexes usually need harsh conditions, and they suffer from poor stability. COFs as photocatalysts for light-induced organic transformations featuring high stability, recyclability and adjustable band structures have been widely utilized in many reactions. Here, we mainly introduce their applications in aerobic oxidation, reductive dehalogenation functionalization and *trans–cis* transition.

3.3.1 Pristine COFs. COFs can act as efficient photocatalysts for aerobic oxidation of amines to imines. Wang *et al.* designed and synthesized a new 2D porphyrin-based sp^2 carbon-linked COF (Por-sp^2c-COF) *via* the Knoevenagel condensation reaction of 5,10,15,20-tetrakis(4-benzaldehyde) porphyrin (*p*-Por-CHO) and 1,4-phenylenediacetonitrile (PDAN).[141] Benefiting from its rigid C=C linkage, Por-sp^2c-COF possessed a permanent porosity and exhibited high chemical stability in various organic solvents and concentrated HCl or NaOH. The prepared Por-sp^2c-COF showed higher photocatalytic activity and better reusability than imine-linked Por-COF for aerobic oxidation of amines to imines under visible light irradiation. Yang *et al.* reported a stable hydrazone-

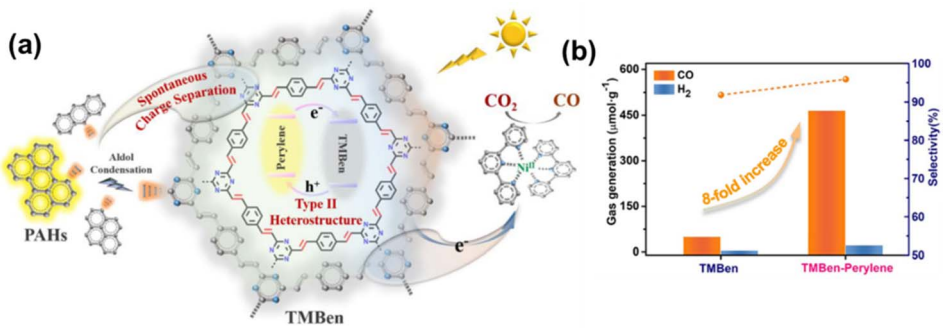

Fig. 13 (a) Schematic illustration of the PAH-functionalized TMBen for photocatalytic CO_2 reduction. (b) A comparison of the amount of product obtained with TMBen and TMBen–perylene after 5 hours of reaction. Reproduced with permission.[130] Copyright 2022, Wiley-VCH.

bridged COF (TFPT-BMTH) with abundant 2-methoxyethoxy groups in the pores.[142] Thanks to the introduction of 2-methoxyethoxy groups that enhance the interlayer interactions and increase the hydrophilic ether content, the TFPT-BMTH COF has several advantages, such as excellent stability, reusability, and hydrophilicity, for the application of photocatalytic oxidation of benzylamine in water. Cao *et al.* constructed three Tp-BTD COF isomers with different stacking modes (AA, AB, and ABC stacking) by reacting 4,7-bis(4-aminophenyl)-2,1,3-benzothiadiazole (BTD) and 2,4,6-triformylphloroglucinol (Tp) at different temperatures and solvent media.[143] They found that different layer stacking led to different ratios of enol and keto forms in these three isomers, which can regulate the photocatalytic production efficiency of Type I reactive oxygen species (superoxide radicals, hydroxyl radicals, and hydrogen peroxide) and Type II reactive oxygen species (singlet oxygen). The Tp-BTD COF with ABC stacking mode exhibited the fastest generation rate of Type I reactive oxygen species, thereby achieving a three-fold higher photocatalytic oxidation efficiency of benzylamine than that of AA stacking and AB stacking isomers. A very recent study by Liu and co-workers developed a new donor–acceptor COF with a wide absorption range from 200 to 900 nm exhibiting a photocatalytic conversion of 99% and a selectivity of 98% in 20 min for selective coupling of benzylamine.[144] Furthermore, by synthesizing a series of donor–acceptor COFs, named JUC-675 to JUC-677, Fang *et al.* realized a photocatalytic system capable of simultaneous production of hydrogen peroxide (H_2O_2) and value-added organic chemical *N*-benzylbenzdiamine (BBAD), maximizing the use of solar energy (Fig. 14). Among them, JUC-675 showed a high selectivity of 99.9% and a yield of 96% for BBAD in oxidative coupling of benzylamine.[145]

Aerobic oxidation of sulfides is feasible by using reactive oxygen species generated by photoexcited COFs. Chen *et al.* synthesized an A_2B_2-Por-COF by a simple acetic acid catalyzed self-condensation reaction.[146] Benefiting from the outstanding light-harvesting capability and favorable photoelectric features of porphyrin, the A_2B_2-Por-COF can effectively oxidize thioanisoles and several methyl phenyl sulfides bearing different substituents with a selectivity of >99% under visible light irradiation. Bai *et al.* fabricated a noodle-like nanofiber AQ-COF with AB stacking mode, which is different from the previously reported spherical AQ-COF_{DMF} with AA stacking mode.[147] The novel micromorphology and stacking module of AQ-COF improved its photocatalytic performance for aerobic oxidation of sulfides to sulfoxides by accelerating electron–hole separation and transfer. Recently, Li *et al.* developed a benzothiadiazole-based COF (TpBTD-COF) *via* solvothermal synthesis using 4,7-bis(4-aminophenyl)-2,1,3-benzothiadiazole (BTD) and 2,4,6-triformylphloroglucinol (Tp). Integrating an electron transfer mediator, (2,2,6,6-tetramethylpiperidin-1-yl)oxyl (TEMPO), significantly improved the photocatalytic performance for aerobic sulfoxidation. TEMPO facilitated smoother electron transfer and dramatically increased conversions, exhibiting over 2.5 times higher activity compared to systems without the mediator. Moreover, TpBTD-COF exhibited exceptional robustness, sustaining multiple reaction cycles with enhanced photocatalytic activity over time.[148] Similarly, Huang *et al.* reported a benzotrithiophene (BTT)-based sp^2 carbon-conjugated COF (BTT-sp^2c-COF) that enabled selective oxidation of organic sulfides with the incorporation of TEMPO. TEMPO efficiently mediated hole transfer from BTT-sp^2c-COF to sulfide substrates, facilitating oxygen incorporation into sulfoxides through electron transfer.[149] Dong *et al.* also synthesized a pyrene-based azine-linked COF (Py-azine-COF) through aldimine condensation between 1,3,6,8-tetrakis(4-formylphenyl)pyrene and hydrazine hydrate. After incorporating TEMPO as a hole mediator, Py-azine-COF exhibited rapid and highly selective aerobic oxidation of various organic sulfides. Mechanistic studies revealed that TEMPO promoted charge separation and cooperated with superoxide radicals formed by oxygen reduction, thereby enhancing overall catalytic efficiency.[150]

COFs are also widely employed in photocatalytic oxidative hydroxylation reactions. In a first report on benzoxazole-based COFs as photocatalysts, reversible/irreversible cascade reactions were employed to synthesize three benzoxazole-based COFs (namely LZU-190, LZU-191, and LZU-192).[151] The obtained COFs demonstrated impressive acid resistivity, alkali resistivity and photostability and an extended light absorption range resulting from their rigid benzoxazole linkage. Among these COFs, LZU-190 showed admirable photoactivity and reusability, which maintained a phenol yield of 99% for more than 20 cycles in photocatalytic oxidative hydroxylation of arylboronic acids tests. Taking advantage of the excellent stability of COFs with a vinylene linkage, Zhang *et al.*

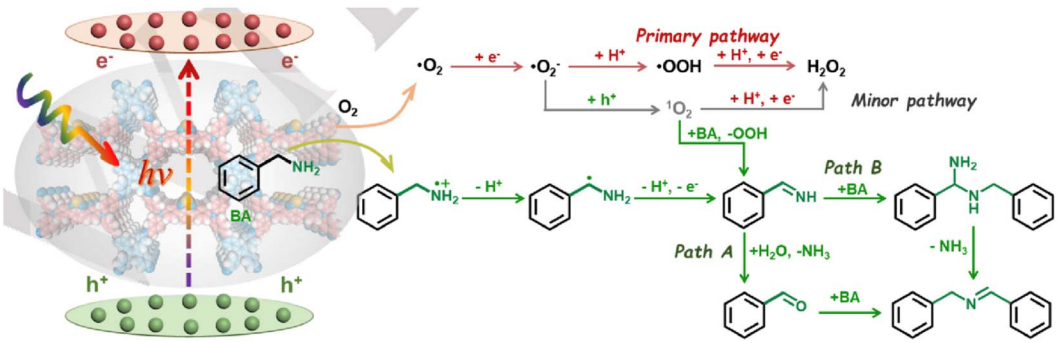

Fig. 14 Reaction mechanism of the photocatalytic H_2O_2 production and BBAD co-production system. Reproduced with permission.[145] Copyright 2024, Wiley-VCH.

synthesized three vinylene-bridged COFs (labeled as COF-*p*-3Ph, COF-*p*-2Ph, and COF-*m*-3Ph) by secondary-amine-catalyzed Knoevenagel condensation.[152] At low loadings, these COFs can effectively and stably oxidize arylboronic acids to phenols driven by visible light. Jiang *et al.* introduced a method to obtain different reactive oxygen species by regulating the excitonic effects in the COFs.[153] In this work, a series of porphyrinic COFs (DhaTph-M, M = 2H, Zn, Ni) were constructed through Schiff-base condensation. The introduction of metal ions into the porphyrin center was found to disrupt the coexistence of excitons and charge carriers under illumination (Fig. 15a). The presence of Zn^{2+} in the porphyrin center increased the transformation of singlet excitons to triplet excitons and promoted the energy transfer process, whereas Ni^{2+} in the porphyrin center facilitated the dissociation of excitons into free carriers and enhanced charge transfer processes. The photocurrent measurements and electrochemical impedance spectroscopy (EIS) results (Fig. 15b and c) show that DhaTph-Ni exhibited the strongest photocurrent response and the lowest charge-transfer resistance among the three COFs, which can be attributed to increased free charge carriers resulting from enhanced exciton dissociation. Conversely, the pronounced electron–hole interaction in DhaTph-Zn resulted in a strong excitonic effect, substantially decreasing free charge carrier generation. Due to the distinct excitonic behavior, DhaTph-Zn and DhaTph-Ni activated oxygen (O_2) to form singlet oxygen ($^1O_2$) and superoxide radicals ($O_2^{\bullet-}$), under visible light excitation. Hence, DhaTph-Zn achieved outstanding performance in selective oxidation of organic sulfides, while DhaTph-Ni realized high photoactivity in hydroxylation of boronic acid.

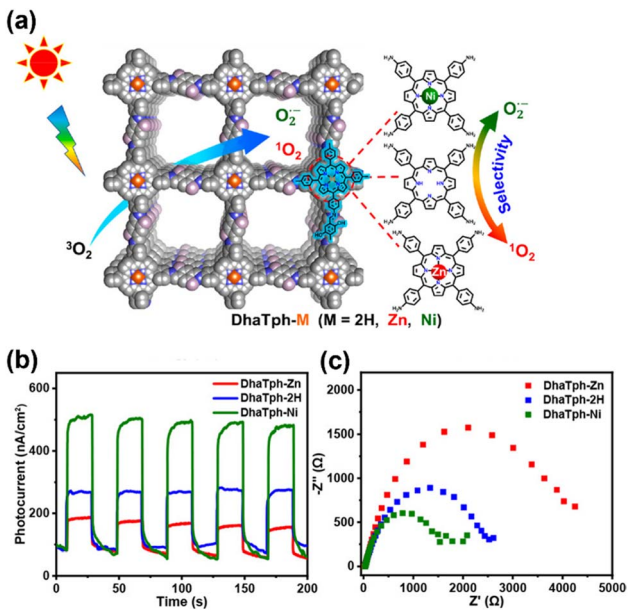

Fig. 15 (a) Schematic displaying DhaTph-M COFs (M = 2H, Zn and Ni) with discriminative oxygen active species selectivity to $^1O_2$ and $O_2^{\bullet-}$ for oxidation of thioanisole and hydroxylation of phenylboronic acid. (b) Photocurrent responses and (c) EIS Nyquist plots for DhaTph-M (M = 2H, Zn, and Ni). Reproduced with permission.[153] Copyright 2020, American Chemical Society.

In addition to aerobic oxidation reactions, COFs can also serve as photocatalysts for reductive dehalogenation reactions. Liu *et al.* prepared a donor–acceptor COF-JLU22 by condensing 1,3,6,8-tetrakis(4-aminophenyl)pyrene and 4,4′-(benzothiadiazole-4,7-diyl)dibenzaldehyde.[154] COF-JLU22 exhibited high activity and recyclability as a heterogeneous photocatalyst for reductive dehalogenation of phenacyl bromide derivatives, which were derived from the large BET specific area, good crystallinity and strong light-harvesting ability. Using a series of [3 + 3] 2D COFs with hexagonal structures but distinct compositions as the model material, Yang *et al.* explored the crucial factors that influence the photocatalytic performance of COFs for the reductive dehalogenation reaction.[155] Among them, OH–TFP–TTA showed the best performance for the photocatalytic reductive dehalogenation reaction. The introduction of –OH groups extended the light absorption range of OH–TFP–TTA. The replacement of TAPB units with triazine units introduced donor–acceptor domains that facilitate charge separation. Considering that the construction of a D–A structure in COFs can accelerate the separation of photogenerated charges, Baeyens *et al.* designed and synthesized three donor–acceptor COFs, BTTZ-por COF, FBQD-por COF and PTBC-por COF, by condensing three electron-deficient aldehydes with electron-donating porphyrin units.[156] The PTBC-Por COF showed the best activity in reductive dehalogenation of 2-bromoacetophenone derivatives due to longer carrier lifetimes, better charge separation and lower charge transfer resistance.

Photocatalytic functionalization of organic molecules is an important approach to acquiring various derivatives with diverse properties. By employing three distinct linkers, Liu *et al.* synthesized three isomorphic pyrene-based COFs to tune their optoelectronic characteristics and band structures.[157] They found that visible light absorption and photogenerated charge transfer processes of COFs were improved by the introduction of 4,4′-([1,2,5]thiadiazolo[3,4-*c*]pyridine-4,7-diyl)-based electron-deficient units. Among the three isomorphic COFs, COF-JLU24 exhibited the highest photocatalytic activity for C-3 functionalization of indoles as well as broad substrate scope and outstanding recyclability as a metal-free photocatalyst. Cai *et al.* constructed a chemically stable olefin-linked 2D-COF (referred to as TTO-COF) by acid-catalyzed aldol condensation of 2,4,6-tris(4-formyl-phenyl)-1,3,5-triazine and 2,4,6-trimethyl-1,3,5-triazine.[158] Owing to high charge carrier conduction efficiency, TTO-COF outperformed imine COFs and g-C_3N_4 in photocatalytic C–H functionalization of arenes and heteroarenes and showed better stability and recyclability.

Achieving a green and economical *trans–cis* (*E–Z*) conversion of alkenes/olefins is of great significance for the synthesis of anticancer drugs, dyes, and scintillators. Banerjee *et al.* reported visible-light-driven *E–Z* transformation of olefins by a COF.[159] The COF (TpTt) was prepared by reacting melamine/1,3,5-triazine-2,4,6-triamine (Tt) and 2,4,6-triformylphloroglucinol (Tp) aldehyde. In these COFs (TpTt), the triazine core forms strong π–π interactions with the *E* alkenes to catalyze *E–Z* photoisomerization and keto functionalities can prolong the lifetime of the excited triplet state. Moreover, the β-ketoenamine linkage gives TpTt high chemical stability. Benefiting

from these features, TpTt can effectively and stably convert *trans*-stilbene to *cis*-stilbene under blue light irradiation.

3.3.2 Post-modified COFs with metals. Enabling metal active sites in COFs is regarded as an effective method to improve their photocatalytic organic transformation performance. Voort *et al.* condensed 4,4′,4″-(1,3,5-triazine-2,4,6-triyl) trianiline (TTA) and acenaphthenequinone (Ace) to form triazine-based Ace-COF (Fig. 16a).[160] The Ace-COF was then decorated with Ni ions (Ace-COF-Ni) by a facile post-synthesis wet impregnation method. The as-prepared Ace-COF-Ni showed broad substrate applicability for visible-light-driven sulfur–carbon cross-coupling reactions with an excellent yield of 79–96%. They proposed a dual-catalytic process in which the Ace-COF cycle and Ni cycle are coupled by electron and radical transfer and synergistically promote organic transformations (Fig. 16b). In the same year, Chen *et al.* immobilized Ni^{II} in the bipyridine sites of a vinyl bridged 2D COF (sp^2c-COF_{dpy}-Ni), realizing highly active and stable photocatalytic C–O coupling from an aryl bromide under visible light irradiation.[161]

In addition, a Pt complex was introduced into COFs for facilitating light driven organic transformations. Alemán *et al.* used a *cis*-[$PtCl_2(DMSO)_2$] precursor to synthesize a Pt(II) hydroxyquinoline complex, which was then covalently bonded with an imine-based COF.[162] The resultant Pt@COF not only brought about high activity for oxidizing sulfides to sulfoxides with a TON of up to 25 000, but also exhibited a turnover number (TON) of 7500 for photohydrodebromination of bromo-derivatives. Beyzavi *et al.* employed 2-(4-formylphenyl)-5-formylpyridine as a COF linker to coordinate with metals for the first time.[163] The COF-UARK-49-Pt photocatalyst with 9.1% Pt loading was obtained by reacting *cis*-[$PtCl_2(DMSO)_2$] and COF-UARK-49 in toluene at 50 °C overnight, which exhibited boosted photocatalytic activity of decarboxylative difluoroalkylation and oxidative cyclization reactions compared to pristine COF-UARK-49.

A dual metalized 2D-COF TpBpy for light driven C-N cross-coupling reactions was introduced by Maji *et al.* A photosensitizing iridium complex and nickel were fixed into the COF pore by chelating with bipyridine sites of the TpBpy COF.[164] The Ni-Ir@TpBpy photocatalyst prevented the formation of nickel-black due to strong metal binding sites, demonstrating superior catalytic performance, durability, and versatility. The authors then employed Ni-Ir@TpBpy-catalyzed C–N coupling reactions to enable the functionalization of amide derivatives and the synthesis of some commercially available drug molecules. Duan *et al.* recently used a bimetallic COF for the

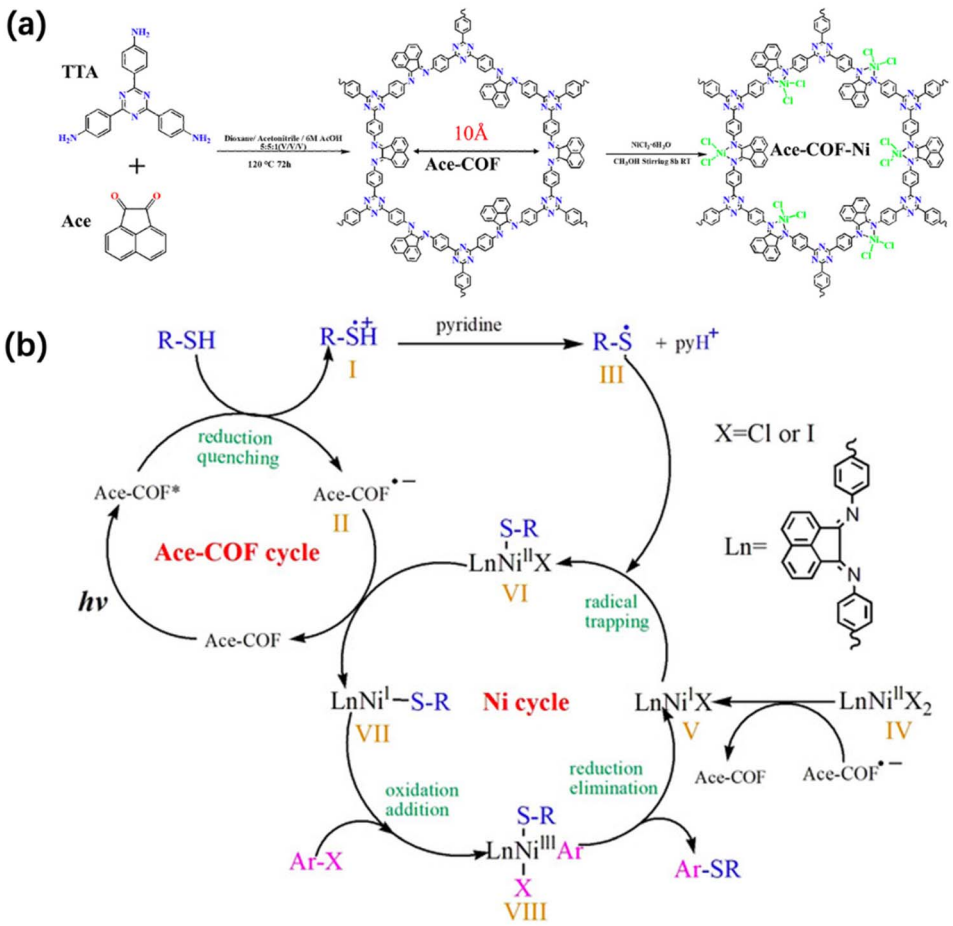

Fig. 16 (a) The synthesis process of Ace-COF-Ni. (b) Proposed mechanism of an Ace-COF-Ni catalyzed sulfur–carbon cross-coupling reaction. Adapted with permission.[160] Copyright 2021, Wiley-VCH.

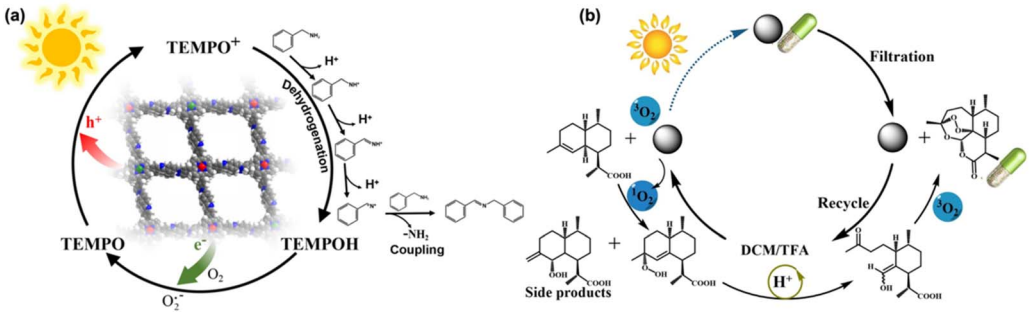

Fig. 17 (a) Schematic diagram of the oxidative coupling mechanism of COF-Sr_2Fe_1 photocatalytic oxidation of benzylamine. Adapted with permission.[165] Copyright 2024, Elsevier. (b) Schematic diagram of the reaction mechanism for producing artemisinin by photocatalytic oxidation. Adapted with permission.[166] Copyright 2024, Wiley-VCH.

oxidative coupling of amines to improve charge separation and catalytic activity. The bimetallic COF-Sr_2Fe_1 was constructed by coordinating Sr^{2+} and Fe^{2+} ions into the porphyrin centers of COF-366. COF-Sr_2Fe_1 achieved a photocatalytic yield of 97% for the oxidative coupling of benzylamine to *N*-benzylbenzaldimine under visible light. This performance significantly surpassed that of monometallic COFs (*e.g.*, COF-Sr at 79% and COF-Fe at 6%). DFT calculations showed that Sr^{2+} enhanced C–N coupling ability, while Fe^{2+} facilitated dehydrogenation. Photogenerated electrons migrate from Fe^{2+} to Sr^{2+}, enhancing charge separation and reaction efficiency (Fig. 17a).[165] Furthermore, Jiang *et al.* expanded the topology of 3D COFs by integrating POSS-based frameworks with porphyrin building blocks. The team synthesized four distinct POSS-linked 3D COFs: POSS-MTFPP-COFs-scu (Co, Zn) and POSS-MTFPP-COFs-sqc (Ni, H_2). Scu topology exhibited triangular and square channels, while sqc featured interpenetrated frameworks. High surface areas were achieved (up to 1726 $m^2\ g^{-1}$ for POSS-ZnTFPP-COF-scu). The frameworks were tested for photocatalytic production of artemisinin, an antimalarial compound. POSS-H_2TFPP-COF-sqc achieved the highest yield (63%) by generating singlet oxygen ($^1O_2$) effectively, which catalyzed the oxidation of dihydroartemisinic acid (Fig. 17b).[166]

3.3.3 COF-based composites. The cooperation of COFs with other catalysts has also been utilized for facilitating photocatalytic organic transformations. Lang *et al.* immobilized (2,2,6,6-tetramethylpiperidin-1-yl)oxyl (TEMPO) into the Por-sp^2c-COF channel,[141] which can convert amines to imines with high activity and selectivity under illumination with a red light-emitting diode (LED).[167] The crystallinity and pore size of Por-sp^2c-COF are essential for this synergistic catalytic process, which is absent in its amorphous counterparts or dye molecules. The authors highlight that the sp^2 –C=C– double bond linkage confers stability to Por-sp^2c-COF under high concentrations of amine. Later, Wang *et al.* used the same porphyrin molecule to react with *p*-phenylenediamine to synthesize imine-based Por-COF.[168] The reported Por-COF only showed mild performance in selective aerobic oxidation of sulfides under white LED irradiation, while the yield of sulfoxides was obviously enhanced by cooperating with the TEMPO catalyst.

Wang *et al.* further introduced a seed growth method to synthesize core–shell NH_2-MIL-125@TAPB-PDA hybrid materials.[169] Specifically, small amounts of terephthaldehyde (PDA) and 1,3,5-tris(4-aminophenyl)benzene (PAPB) precursors were first added into NH_2-MIL-125 suspension to generate COF seeds on the NH_2-MIL-125 surface. Controlled amounts of PDA and PAPB were subsequently added to obtain NH_2-MIL-125@TAPB-PDA photocatalysts with different COF shell thicknesses. The best yield of 94.7% for photo-oxidation of benzyl alcohols to benzaldehydes was achieved by NH_2-MIL-125@TAPB-PDA-3 with a COF shell thickness of ~20 nm, which was a 2.5- and 15.5-fold enhancement compared to NH_2-MIL-125 and TAPB-PDA COF, respectively. Huang *et al.* designed and prepared COF/CdS composites for oxidizing benzyl alcohols to benzaldehydes.[170] The COF was prepared by condensation of terephthalaldehyde and 1,3,5-tris(4-aminophenyl)benzene. The synthesis of COF/CdS composites with varying CdS contents was achieved by reaction with cadmium acetate, thioacetamide and COF with different mass ratios. A series of COF/CdS photocatalysts were obtained and denoted as COF/CdS-1, COF/CdS-2, COF/CdS-3 and COF/CdS-4, respectively. COF/CdS-3 gave the highest benzaldehyde yield of 97.1%, which is 2.5 and 15.9 times that of pure CdS and COF, respectively. The boosted photocatalytic oxidation efficiency was attributed to the improved electron–hole separation in the COF/CdS heterojunction. Kuang *et al.* recently combined $Cs_2AgBiCl_6$ (CABC) with a semi-conductive covalent organic framework (C_4N) to form a type II heterojunction with staggered band alignment, creating an improved photocatalyst (Fig. 18a).[171] In this heterojunction, C_4N provided heterogeneous nucleation sites for CABC crystal growth and the oxygen affinity of C_4N enhanced aerobic reactivity. The combination enabled better separation of charge carriers. The optimal CABC/C_4N heterojunction achieved 100% thioanisole conversion after 6 hours. This was 2.2 times better than that of pure CABC and 7.7 times better than that of pure C_4N. The catalyst showed good stability over five cycles (Fig. 18b and c). Tan *et al.* adopted an *in situ* encapsulation strategy to develop a novel coralloid $W_{18}O_{49}$@TpPa-H S-scheme heterojunction for efficient photocatalytic aerobic oxidation.[172] In this heterojunction, $W_{18}O_{49}$ nanobundles acted as "coral bones" wrapped in a branched TpPa-H structure and exhibited broad light absorption across UV-visible-NIR regions. The optimized $W_{18}O_{49}$@TpPa-H-0.1 achieved a benzylamine conversion rate of 99% in 4 hours

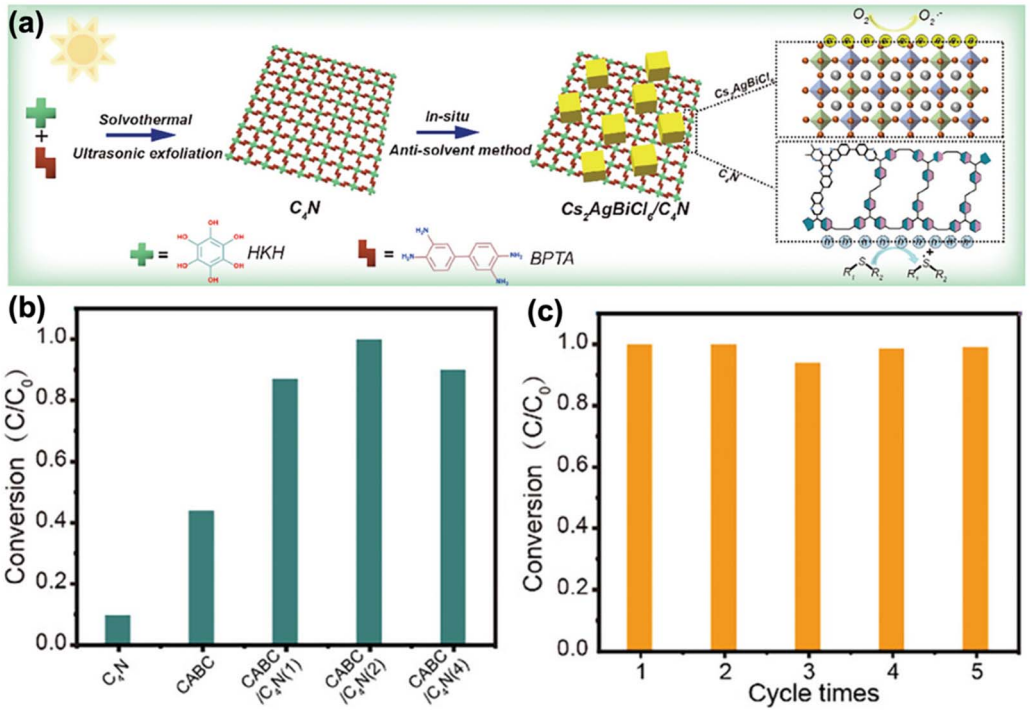

Fig. 18 (a) Schematic of synthesis path of the CABC/C_4N heterojunction. (b) Comparison of photocatalytic oxidation properties of thioesters. (c) Photocatalytic cycle stability of CABC/C_4N. Adapted with permission.[171] Copyright 2024, Wiley-VCH.

with an imide product selectivity of 99%. The photocatalytic performance is 9.9 times better than that of pure $W_{18}O_{49}$ and 2.8 times better than that of pure TPA-H. $W_{18}O_{49}$@TpPa-H-0.1 was effective even under 740 nm light and showed good stability over 5 reaction cycles. The research represents an important advancement in developing efficient photocatalysts for organic synthesis, particularly in the selective oxidation of amines to imines under mild conditions solely using light and air as the reagents.

3.4 Photocatalytic hydrogen peroxide production

H_2O_2 is a versatile chemical widely used as an antimicrobial disinfectant, bleach, and oxidizing agent in chemical synthesis. Compared with traditional production methods such as the anthraquinone oxidation reaction, photocatalytic synthesis provides an environmentally friendly and cost-effective alternative that uses solar energy and water to reduce pollution. COFs composed of earth-abundant elements like C, H and N show promise as new generation photocatalysts for H_2O_2 production. In addition to their strong visible light absorption, efficient photo-induced carrier separation, and tunable and diverse structures, COFs allow the formation of intermediates suitable for H_2O_2 synthesis while hindering its decomposition. Table 3 summarizes the photocatalytic H_2O_2 production performance of some COF-based photocatalysts.

3.4.1 Pristine COFs. The pioneering demonstration of photocatalytic H_2O_2 production using highly crystalline covalent organic frameworks was reported by Van Der Voort and coworkers.[173] The diarylamine (donor) moiety within the COF structure conferred robust reductive capabilities, resulting in a H_2O_2 formation rate of 234.5 μmol h^{-1} g^{-1}. Since then, many donor–acceptor COFs have been designed and synthesized for photocatalytic hydrogen peroxide production and have well-defined and separated oxidation–reduction centers, exhibiting better photogenerated charge separation and prolonged carrier lifetime.[174–177] In a representative study, tetrathiafulvalene (TTF) and benzothiazole (BT) were covalently bonded to synthesize TTF-BT-COF, in which TTF acts as a photo-oxidation site and BT acts as a photo-reduction site (Fig. 19a).[174] Under light excitation, the photo-induced charge carriers became spatially separated, where the holes were concentrated in the TTF unit for the water oxidation reaction (WOR) and the electrons were accumulated in the BT unit for the oxygen reduction reaction (ORR). The theoretical calculations showed that TTF and BT were beneficial to the adsorption of reaction intermediates *OH and *OOH, respectively, which reduced the reaction energy barrier of the WOR and ORR. Among the three COFs, TTF-BT-COF exhibited the best photocatalytic performance with a H_2O_2 production rate of up to 1380 μM h^{-1} (Fig. 19b). Furthermore, TTF-BT-COF showed high stability over three photocatalytic cycles (Fig. 19c). Electron-deficient triazine units are typically used as acceptors in the construction of D–A COFs.[175–177] For example, Mi and coworkers synthesized a vinylene-linked EBA-COF by integrating triazine and acetylene, exhibiting a H_2O_2 production rate of 1830 μmol h^{-1} g^{-1}.[175] The H_2O_2 synthesis in a $2e^-$ pathway was accelerated due to improved charge separation and transport in D–A configurations. The triazine units have also been covalently linked with electron-donating phenyl groups to construct D–A structures.[176] An appropriate number

Table 3 Summary of photocatalytic H_2O_2 evolution rates of COF-based photocatalysts

Samples	Irradiation conditions	Solvent system	H_2O_2 production rate (μmol h^{-1} g^{-1})	Ref.
TAPD-(Me)2 COF	700 nm > λ > 420 nm	H_2O : EtOH (1 : 9, v/v)	234.52	173
TTF-BT-COF	AM 1.5	H_2O	690	174
EBA-COF	λ > 420 nm	H_2O : EtOH (9 : 1, v/v)	1830	175
COF-N32	λ > 420 nm	H_2O	605	176
TaptBtt	λ > 420 nm	H_2O	1407	177
TZ-COF	λ > 420 nm	H_2O	268	178
COF-2CN	λ > 420 nm	H_2O	1601	179
DVA-COF	λ = 420 nm	H_2O : BA (9 : 1, v/v)	8450	180
TF50-COF	λ > 400 nm	H_2O : EtOH (9 : 1, v/v)	1739	181
COF-TfpBpy	λ > 420 nm	H_2O	694	182
COF-BPDA-DTP	λ > 420 nm	H_2O	1164	183
TiCOF-spn	780 nm ≥ λ ≥ 420 nm	H_2O	489.94	184
COF-NUST-16	λ > 420 nm	H_2O : EtOH (9 : 1, v/v)	1081	185
CoPcF16	λ > 400 nm	H_2O : EtOH (9 : 1, v/v)	2096	186
TAPT-TFPA COFs	AM 1.5	H_2O	2143	187
ZnO/TpPa-Cl	AM 1.5	H_2O : EtOH (9 : 1, v/v)	2443	188
TiO_2/BTTA	780 nm > λ > 350 nm	FAL	1480	189
CDs@CTFs	λ ≥ 420 nm	H_2O	535.41	190
$Bi_4O_5Br_2$/TTD-COF	LED (400–700 nm)	H_2O	5221	191
COF-ZCS	λ ≥ 420 nm	H_2O	5171	192
$CsPbBr_3$/CTFs	λ = 420 nm	H_2O	1680	193
$ZnIn_2S_4$/TpPa-1	780 nm > λ > 400 nm	H_2O : EtOH (9 : 1, v/v)	1032	194
WO_3/Tp-TAPB	λ > 420 nm	H_2O	1488.4	195
CTF-1-G/WS_2	λ > 420 nm	H_2O	156	196

of phenyl groups improved the triazine N 2p states and optimized intramolecular polarity, thereby lowering the energy barrier for H_2O activation and ultimately achieving efficient H_2O_2 production. In addition to judiciously choosing suitable donor–acceptor pairs, the linkage microenvironment also considerably influences the charge transfer efficiency. Wang *et al.* discovered that TZ-COF with a D–π–A structure and thiazole linkages facilitated more effective pathways for charge transport, thus achieving more effective H_2O_2 generation than the oxazole-linked OZ-COF and imidazole-linked IZ-COF.[178]

Modification and doping of COFs constitute pivotal avenues for enhancing the performance of COFs in photocatalytic H_2O_2

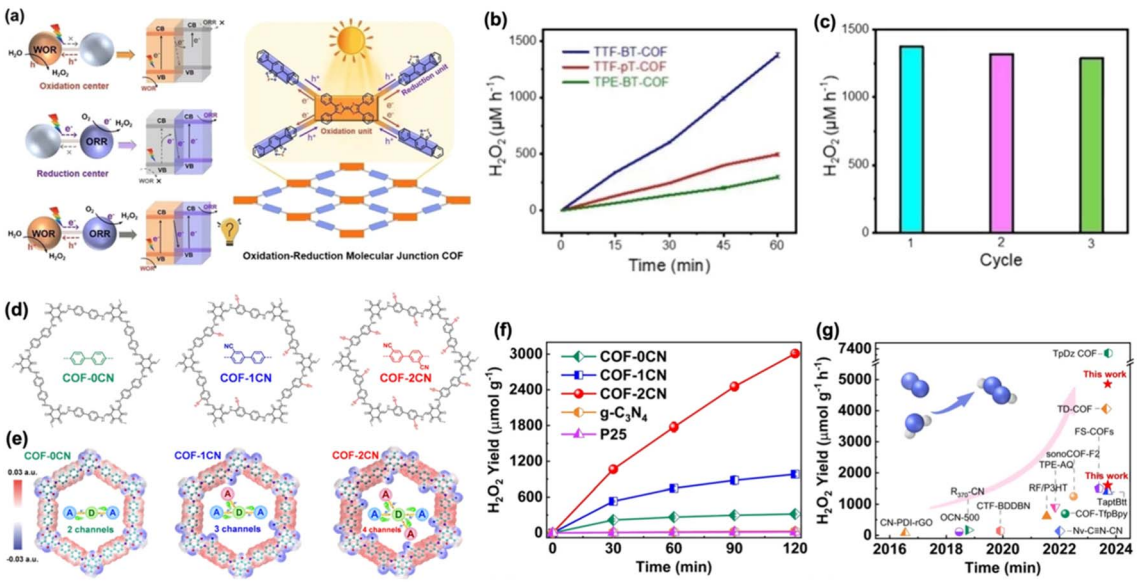

Fig. 19 (a) The TTF-BT-COF with an oxidation–reduction molecular junction produces H_2O_2 *via* the ORR and WOR simultaneously. (b) Photocatalytic H_2O_2 production activity of the three COFs. (c) Photocatalytic cycle stability of TTF-BT-COF. Adapted with permission.[174] Copyright 2022, Wiley-VCH. (d) Chemical structure of COF-0CN, COF-1CN and COF-2CN. (e) Electrostatic potential distribution of COF-0CN, COF-1CN and COF-2CN. (f) Photocatalytic synthesis of H_2O_2 from COFs, g-C_3N_4 and P25. (g) Comparison of the performance of COF-2CN and other photocatalysts. Adapted with permission.[179] Copyright 2024, Wiley-VCH.

generation. Ni *et al.* synthesized three COFs, designated as COF-0CN, COF-1CN, and COF-2CN, each featuring a varying degree of cyano group modification (Fig. 19d).[179] A positive correlation was observed between the number of cyano groups and the efficiency of charge separation and transport within the COFs. Experimental results and theoretical calculations indicated that cyano group modifications augmented the number of charge transfer pathways between donor and acceptor moieties, thereby facilitating charge separation and transport processes (Fig. 19e). Additionally, the incorporation of dicyano modifications was found to reduce the energy barrier for the two-electron water oxidation reaction. Finally, COF-2CN achieved a high H_2O_2 production rate of 1601 μmol h^{-1} g^{-1} under visible light irradiation using only water and oxygen as reactants (Fig. 19f). This performance was superior to that of most conventional photocatalysts and most recently reported catalysts (Fig. 19g). Chen *et al.* demonstrated that the anchored vinyl groups in DVA-COF not only broadened the light absorption spectrum but also accelerated charge separation and transfer efficiency, which consequently promoted the generation of H_2O_2 *via* the $2e^-$ ORR pathway.[180] By means of fluorine substitution, plenty of Lewis acid sites were introduced into TF_{50}-COF, which helped fine-tune the electronic structure of proximate carbon atoms, promote O_2 adsorption, extend the light-harvesting range and elevate charge separation efficiency.[181] The protonation of bipyridine units in COF-TfpBpy was believed to promote the $2e^-$ WOR and further facilitate the formation of endoperoxide intermediate species, which strengthened Yeager-type oxygen adsorption on COF-TfpBpy, accelerating the one-step $2e^-$ ORR process.[182] Consequently, COF-TfpBpy exhibited a high solar-to-chemical conversion efficiency of 0.57% at 298 K. Kong and co-workers developed a molecular engineering strategy to fabricate three imine-linked alkyne-containing COFs (COF-BPDA-DTP, -BD, and -PA) that had similar molecular structures but different lengths of linkers.[183] They found that longer linkers potentially contribute to a more negative conductive band energy level, increased specific surface area, and enhanced charge separation efficiency. Among the three COFs, COF-BPDA-DTP with the longest linker length exhibited the highest H_2O_2 production rate of 1164 μmol h^{-1} g_{cat}^{-1}.

The layered structure of 2D COFs limits the exposure of active sites, which diminishes photocatalytic efficiency, whereas 3D COFs retain intrinsic precursor properties with non-overlapping π-planes. TiCOF-spn integrated a photoactive titanium center and triazine units in a 3D crystalline porous structure, exhibiting a photocatalytic H_2O_2 production rate of 489.9 μmol h^{-1} g^{-1}.[184] Zhang *et al.* constructed a 3D COF (COF-NUST-16) with *tty* topology achieving a photocatalytic H_2O_2 production rate of 1081 μmol h^{-1} g^{-1}.[185] Notably, its photocatalytic performance was over 4 times greater than that of COF-NUST-17 – a 2D COF with a similar structure, highlighting better active site accessibility and mass transfer of its 3D framework in boosting photocatalytic activity.

3.4.2 Post-modified COFs with metals. Phthalocyanine (Pc) has the potential to synthesize 2D COFs with a fully conjugated structure. CoPc with the $M–N_4$ configuration has high selectivity and activity for the $2e^-$ ORR. Jiang *et al.* synthesized CoPc-BTM-COF and CoPc-DAB-COF *via* the nucleophilic substitution reaction of hexadecafluorophthalocyaninato cobalt(II) ($CoPcF_{16}$) with 1,2,4,5-benzenetetramine (BTM) or 3,3′-diaminobenzidine (DAB), respectively.[186] Impressively, CoPc-BTM-COF with a Co content of 6.41% demonstrated a record-high H_2O_2 rate of 2096 μmol h^{-1} g^{-1} and an outstanding apparent quantum yield of 7.2% at 630 nm. The high photocatalytic activity of CoPc-BTM-COF can be attributed to its excellent light absorption capability as well as enhanced charge separation and transport efficiency. Furthermore, the Co atoms within its structure served as highly active sites for the $2e^-$ oxygen reduction reaction to produce H_2O_2, exhibiting faster reaction dynamics that further contributed to its superior photocatalytic performance. Guo *et al.* reported fluorinated COFs, namely TAPT-TFPA COFs,[187] in which strong electronegative fluorine helps to stabilize Pd metal-isolated clusters (ICs) by the enhanced metal–support interaction and optimize the d-band center of the Pd ICs. Consequently, TAPT-TFPA COFs@Pd ICs showed a high photocatalytic H_2O_2 production rate of 2143 μmol h^{-1} g^{-1} and extraordinary stability over 100 h.

3.4.3 COF-based composites. Rapid recombination of photogenerated carriers significantly limits the photocatalytic activity of COFs, which can be overcome by introducing another semiconductor with appropriate energy band positions to construct a built-in electric field. Zhang *et al.* synthesized a ZnO/TpPa-Cl S-scheme photocatalyst by a simple electrostatic self-assembly method.[188] This composite material has increased light-harvesting capability, facilitated reactant adsorption, enhanced redox ability, and improved charge separation efficiency. Consequently, the ZnO/TpPa-Cl composite exhibited a photocatalytic H_2O_2 production rate of 2443 μmol h^{-1} g^{-1}, which is 3.3 and 8.7 times that of the ZnO NPs and TpPa-Cl, respectively. TiO_2/BTTA S-scheme core–shell hybrids were successfully fabricated by *in situ* growth of BTTA on the surface of TiO_2 nanofibers.[189] The S-scheme heterojunction can both enhance charge carrier separation and retain the redox ability of the photocatalyst. The authors cleverly leveraged this feature by employing a TiO_2/BTTA composite to simultaneously catalyze H_2O_2 evolution and furoic alcohol conversion reactions. Hu *et al.* used carbon dots (CDs) as heterogeneous nucleating agents to accelerate the production of CTFs and simultaneously obtained a special CDs@CTF sandwich structure.[190] CDs in the interlamination of CTFs served as hole traps and longer wavelength light harvesting complexes, enabling enhanced H_2O_2 production efficiency by 22.6-fold. Tang *et al.* prepared a heterojunction photocatalyst (denoted as BIT) by combining a bismuth-based semiconductor ($Bi_4O_5Br_2$) with TTD-COF – a COF featuring triazine and pyridine units.[191] The S-scheme heterojunction generates a built-in electric field, which promotes efficient charge separation and migration by transferring electrons from $Bi_4O_5Br_2$ to TTD-COF under light irradiation (Fig. 20a). BIT6 achieved a H_2O_2 production rate of 5221 μmol h^{-1} g^{-1}, which is 20 times higher than that of $Bi_4O_5Br_2$ and 1.7 times higher than that of TTD-COF alone (Fig. 20b). Jiang *et al.* developed a novel S-scheme heterojunction by integrating a tetrathiafulvalene-based COF (TT-COF) with ZnCdS (ZCS) quantum dots to enhance carrier separation and improve

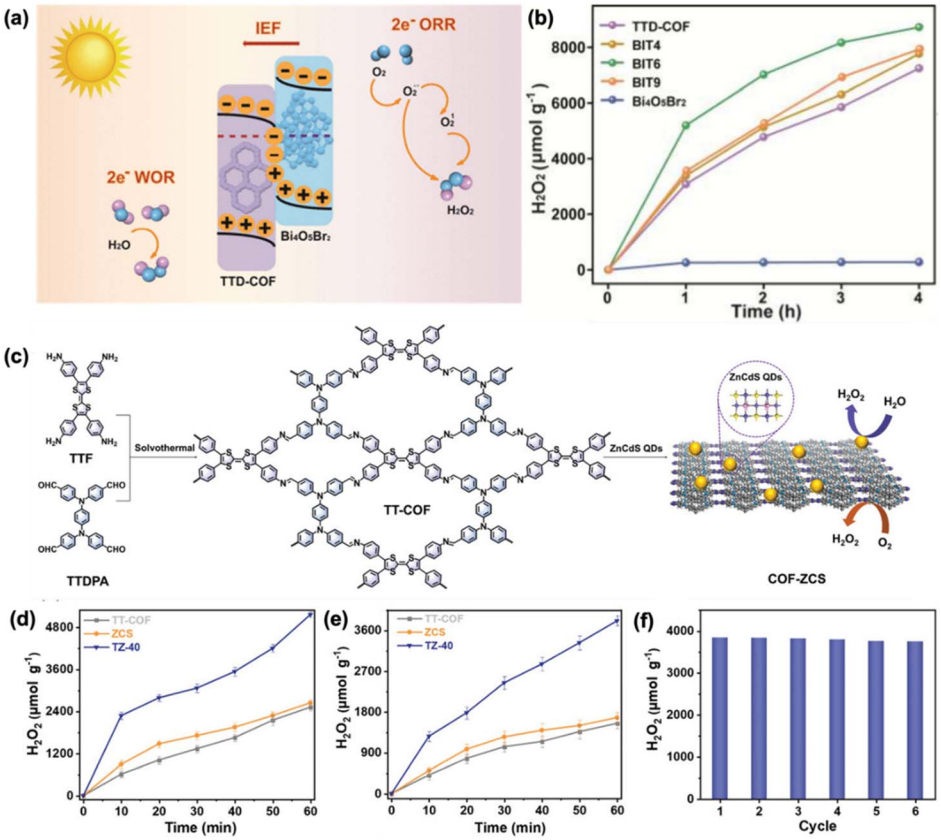

Fig. 20 (a) Schematic diagram of the mechanism of photocatalytic H_2O_2 production in an S-scheme heterojunction. (b) Rate of photocatalytic hydrogen peroxide production by BIT and other catalysts. Adapted with permission.[191] Copyright 2024, American Chemical Society. (c) Synthesis diagram of the TT-COF/ZCS composite. Photocatalytic production of H_2O_2 in (d) oxygen and (e) air environments for TT-COF, ZCS, and TZ-40. (f) Photocatalytic cycle stability of TZ-40. Adapted with permission.[192] Copyright 2024, Wiley-VCH.

redox ability (Fig. 20c).[192] In an oxygen atmosphere, the optimized composite (TZ-40) achieved an H_2O_2 yield of 5171 μmol h^{-1} g^{-1}, significantly higher than that of TT-COF (2520 μmol h^{-1} g^{-1}) or ZCS (2647 μmol h^{-1} g^{-1}) (Fig. 20d). Under ambient air, the H_2O_2 yield reached 3816 μmol g h^{-1} g^{-1}, demonstrating versatility in practical applications (Fig. 20e). The catalyst displayed well-maintained performance over six cycles with minimal structural changes (Fig. 20f). More composites, such as $CsPbBr_3$/CTFs,[193] $ZnIn_2S_4$/TpPa-1,194 WO_3/Tp-TAPB,[195] and CTF-1-G/WS_2,[196] have been constructed and achieved efficient photocatalytic production of H_2O_2.

4 Conclusion and perspective

COFs are novel porous materials constructed from covalently linking organic building blocks and are regarded as one of the most promising materials for heterogeneous photocatalysis because of their molecular backbones that are beneficial for light harvesting and promoting charge separation and transport. On the one hand, molecular chromophores with excellent light harvesting capability can be selected to build the backbone of COFs. On the other hand, conjugated architecture, both in-plane and through stacking, could promote redshift of light absorption, which allows harvesting more portions of solar light. At the same time, the conjugated and crystalline structure of COFs can also facilitate charge transport, prevent charge recombination, and increase charge carrier mobility. Furthermore, covalent bonds of COFs make them stable and robust, which is very important for their applications in photocatalysis. Benefiting from the structural diversity, designability and tunability of COFs, multiple favorable properties can be integrated into one material for photocatalytic applications.

In this review, we start with a brief discussion of the structural design concepts of COFs and highlight the merits of COFs as photocatalysts. We then introduce the progress of COFs as photocatalysts in photocatalytic H_2 production, CO_2 reduction, organic transformations, and H_2O_2 production in the last five years. Pure COFs exhibit tunable band structures and excitonic behavior and customizable surface properties such as the modification of hydrophilic groups to improve hydrophilicity. Abundant metal anchoring sites such as bipyridine and porphyrin units allow COFs to easily load well-defined metal active sites to realize higher photocatalytic performance. Simultaneously, strong coordination or chelation between the metals and COFs enables long-term stability of metal sites. In addition, higher photocatalytic efficiencies are achieved by combining COFs with other semiconductor materials such as TiO_2, CdS, g-C_3N_4 and MOFs. COF-based composites synergize

the benefits of both components and form a type II or Z scheme heterojunction that facilitates the charge separation efficiency.

Despite significant progress in the photocatalytic applications of COFs, some urgent challenges remain to be addressed. Firstly, the solar to hydrogen (STH) and solar to fuel (STF) efficiencies of COFs are not yet satisfactory, especially in the absence of sacrificial agents. Only a few COFs have been reported to achieve high efficiency in photocatalytic H_2 production and CO_2 reduction using water as the hole scavenger. It is highly desired to construct COFs with suitable band diagrams for simultaneous driving oxidation and reduction half-reactions in one photocatalyst, *i.e.* overall water splitting. Secondly, conventional synthesis methods of COFs are restricted by harsh reaction conditions. Developing synthetic procedures with mild conditions, low cost, and high yield is imperative for large-scale fabrication of COFs. Even though some COFs with specific linkages can be synthesized on a large scale, there is still a lack of synthetic methods for the fabrication of most COF materials. Lastly, the in-depth mechanism of COF-based photocatalysts is still elusive. Steady and time-resolved spectroscopy can be employed to explore the formation, separation, and recombination of photogenerated carriers. Various *in situ* techniques such as *in situ* Fourier transform infrared spectroscopy and X-ray photoelectron spectroscopy can be utilized to identify reaction intermediates and study active centers to guide the design of new COFs. Although many problems are yet to be overcome, large-scale applications of COF photocatalysis can still be foreseen through continuous research efforts to overcome these challenges.

Data availability

No primary research results, software or code have been included, and no new data were generated or analysed as part of this review.

Conflicts of interest

The authors declare no competing financial interests.

Acknowledgements

We acknowledge the financial support from the Science and Technology Project of Jiangsu Province (BZ2022056). We also acknowledge the support from the Eastern Institute of Technology, Ningbo, and Shanghai Institute of Organic Chemistry.

References

1 D. Coumou, G. Di Capua, S. Vavrus, L. Wang and S. Wang, *Nat. Commun.*, 2018, **9**, 2959.
2 D. Shindell and C. J. Smith, *Nature*, 2019, **573**, 408–411.
3 J. Zhang, W. Tian, M. P. Chipperfield, F. Xie and J. Huang, *Nat. Clim. Change*, 2016, **6**, 1094–1099.
4 N. S. Lewis, *Science*, 2007, **315**, 798–801.
5 S. Berardi, S. Drouet, L. Francàs, C. Gimbert-Suriñach, M. Guttentag, C. Richmond, T. Stoll and A. Llobet, *Chem. Soc. Rev.*, 2014, **43**, 7501–7519.
6 D. K. Dogutan and D. G. Nocera, *Acc. Chem. Res.*, 2019, **52**, 3143–3148.
7 A. Fujishima and K. Honda, *Nature*, 1972, **238**, 37–38.
8 Q. Guo, Z. Ma, C. Zhou, Z. Ren and X. Yang, *Chem. Rev.*, 2019, **119**, 11020–11041.
9 M. D. Regulacio and M.-Y. Han, *Acc. Chem. Res.*, 2016, **49**, 511–519.
10 L. Wang, Y. Zhang, L. Chen, H. Xu and Y. Xiong, *Adv. Mater.*, 2018, **30**, 1801955.
11 C. Zhao, Z. Chen, R. Shi, X. Yang and T. Zhang, *Adv. Mater.*, 2020, **32**, 1907296.
12 X. Wang, K. Maeda, A. Thomas, K. Takanabe, G. Xin, J. M. Carlsson, K. Domen and M. Antonietti, *Nat. Mater.*, 2009, **8**, 76–80.
13 P. Kuhn, M. Antonietti and A. Thomas, *Angew. Chem., Int. Ed.*, 2008, **47**, 3450–3453.
14 V. Coropceanu, J. Cornil, D. A. da Silva Filho, Y. Olivier, R. Silbey and J.-L. Brédas, *Chem. Rev.*, 2007, **107**, 926–952.
15 S. Tao and D. Jiang, *CCS Chem.*, 2021, **3**, 2003–2024.
16 Z.-J. Lin, S. A. Mahammed, T.-F. Liu and R. Cao, *ACS Cent. Sci.*, 2022, **8**, 1589–1608.
17 H. Wang, H. Wang, Z. Wang, L. Tang, G. Zeng, P. Xu, M. Chen, T. Xiong, C. Zhou and X. Li, *Chem. Soc. Rev.*, 2020, **49**, 4135–4165.
18 B. Wang, R.-B. Lin, Z. Zhang, S. Xiang and B. Chen, *J. Am. Chem. Soc.*, 2020, **142**, 14399–14416.
19 J. Cao, Z. Yang, W. Xiong, Y. Zhou, Y. Wu, M. Jia, C. Zhou and Z. Xu, *Coord. Chem. Rev.*, 2021, **439**, 213924.
20 T. Zhang and W. Lin, *Chem. Soc. Rev.*, 2014, **43**, 5982–5993.
21 R.-B. Lin, Y. He, P. Li, H. Wang, W. Zhou and B. Chen, *Chem. Soc. Rev.*, 2019, **48**, 1362–1389.
22 S. Kitagawa, *Chem. Soc. Rev.*, 2014, **43**, 5415–5418.
23 X. Feng, X. Ding and D. Jiang, *Chem. Soc. Rev.*, 2012, **41**, 6010–6022.
24 A. P. Cote, A. I. Benin, N. W. Ockwig, M. O'Keeffe, A. J. Matzger and O. M. Yaghi, *Science*, 2005, **310**, 1166–1170.
25 C. S. Diercks and O. M. Yaghi, *Science*, 2017, **355**, eeal1585.
26 Y. Zeng, R. Zou and Y. Zhao, *Adv. Mater.*, 2016, **28**, 2855–2873.
27 X. Zhao, P. Pachfule, S. Li, T. Langenhahn, M. Ye, C. Schlesiger, S. Praetz, J. Schmidt and A. Thomas, *J. Am. Chem. Soc.*, 2019, **141**, 6623–6630.
28 X. Liu, D. Huang, C. Lai, G. Zeng, L. Qin, H. Wang, H. Yi, B. Li, S. Liu and M. Zhang, *Chem. Soc. Rev.*, 2019, **48**, 5266–5302.
29 S. Liu, T. Qian, M. Wang, H. Ji, X. Shen, C. Wang and C. Yan, *Nat. Catal.*, 2021, **4**, 322–331.
30 W. Zhang, L. Chen, S. Dai, C. Zhao, C. Ma, L. Wei, M. Zhu, S. Y. Chong, H. Yang and L. Liu, *Nature*, 2022, **604**, 72–79.
31 N. Keller and T. Bein, *Chem. Soc. Rev.*, 2021, **50**, 1813–1845.
32 Y.-N. Gong, X. Guan and H.-L. Jiang, *Coord. Chem. Rev.*, 2023, **475**, 214889.

33 S. Wan, J. Guo, J. Kim, H. Ihee and D. Jiang, *Angew. Chem., Int. Ed.*, 2008, **47**, 8826–8830.
34 Y. Li, X. Song, G. Zhang, L. Wang, Y. Liu, W. Chen and L. Chen, *ChemSusChem*, 2022, **15**, e202200901.
35 H. L. Nguyen and A. Alzamly, *ACS Catal.*, 2021, **11**, 9809–9824.
36 P. Costa, A. Vega-Peñaloza, L. Cognigni and M. Bonchio, *ACS Sustain. Chem. Eng.*, 2021, **9**, 15694–15721.
37 T. Banerjee, K. Gottschling, G. Savasci, C. Ochsenfeld and B. V. Lotsch, *ACS Energy Lett.*, 2018, **3**, 400–409.
38 E. Jin, M. Asada, Q. Xu, S. Dalapati, M. A. Addicoat, M. A. Brady, H. Xu, T. Nakamura, T. Heine, Q. Chen and D. Jiang, *Science*, 2017, **357**, 673–676.
39 A. Acharjya, P. Pachfule, J. Roeser, F.-J. Schmitt and A. Thomas, *Angew. Chem., Int. Ed.*, 2019, **58**, 14865–14870.
40 S. Bi, C. Yang, W. Zhang, J. Xu, L. Liu, D. Wu, X. Wang, Y. Han, Q. Liang and F. Zhang, *Nat. Commun.*, 2019, **10**, 2467.
41 M. S. Lohse and T. Bein, *Adv. Funct. Mater.*, 2018, **28**, 1705553.
42 N. Keller, M. Calik, D. Sharapa, H. R. Soni, P. M. Zehetmaier, S. Rager, F. Auras, A. C. Jakowetz, A. Görling, T. Clark and T. Bein, *J. Am. Chem. Soc.*, 2018, **140**, 16544–16552.
43 N. Keller, D. Bessinger, S. Reuter, M. Calik, L. Ascherl, F. C. Hanusch, F. Auras and T. Bein, *J. Am. Chem. Soc.*, 2017, **139**, 8194–8199.
44 Z. Li, T. He, Y. Gong and D. Jiang, *Acc. Chem. Res.*, 2020, **53**, 1672–1685.
45 X. Guan, F. Chen, Q. Fang and S. Qiu, *Chem. Soc. Rev.*, 2020, **49**, 1357–1384.
46 X. Guan, Q. Fang, Y. Yan and S. Qiu, *Acc. Chem. Res.*, 2022, **55**, 1912–1927.
47 J. Ding, X. Guan, J. Lv, X. Chen, Y. Zhang, H. Li, D. Zhang, S. Qiu, H. L. Jiang and Q. Fang, *J. Am. Chem. Soc.*, 2023, **145**, 3248–3254.
48 R. M. Zhu, Y. Liu, W. K. Han, J. D. Feng, J. Zhang, H. Pang, J. Zhang and Z. G. Gu, *Angew. Chem., Int. Ed.*, 2025, **64**, e202412890.
49 N. Li, J. Zhang, X. Xie, K. Wang, D. Qi, J. Liu, Y. Q. Lan and J. Jiang, *Nat. Commun.*, 2025, **16**, 1106.
50 L. Y. Qin, C. D. Ma, J. Zhang and T. H. Zhou, *Adv. Funct. Mater.*, 2024, **34**, 2414086.
51 C. Qian, L. Feng, W. L. Teo, J. Liu, W. Zhou, D. Wang and Y. Zhao, *Nat. Rev. Chem*, 2022, **6**, 881–898.
52 W. X. Li, Y. X. Wang, L. Li, X. Y. Huang, M. D. Liu, B. Gui, X. J. Lang and C. Wang, *Chin. J. Struct. Chem.*, 2024, **43**, 138196.
53 E. Q. Jin, M. Asada, Q. Xu, S. Dalapati, M. A. Addicoat, M. A. Brady, H. Xu, T. Nakamura, T. Heine, Q. H. Chen and D. L. Jiang, *Science*, 2017, **357**, 673–676.
54 H. Zhuang, C. Guo, J. Huang, L. Wang, Z. Zheng, H. N. Wang, Y. Chen and Y. Q. Lan, *Angew. Chem., Int. Ed.*, 2024, **63**, e202404941.
55 J. Dong, X. Han, Y. Liu, H. Li and Y. Cui, *Angew. Chem., Int. Ed.*, 2020, **59**, 13722–13733.
56 M.-H. Li, C. Xu and Y.-W. Yang, *Coord. Chem. Rev.*, 2024, **512**, 215894.
57 L. Sun, M. Lu, Z. Yang, Z. Yu, X. Su, Y. Q. Lan and L. Chen, *Angew. Chem., Int. Ed.*, 2022, **61**, e202204326.
58 B. Zhang, H. Li, Y. Kang, K. Yang, H. Liu, Y. Zhao and S. Qiao, *Adv. Funct. Mater.*, 2024, **35**, 2416958.
59 M. Zhang, P. Huang, J. P. Liao, M. Y. Yang, S. B. Zhang, Y. F. Liu, M. Lu, S. L. Li, Y. P. Cai and Y. Q. Lan, *Angew. Chem., Int. Ed.*, 2023, **62**, e202311999.
60 S. Wang, Q. Sun, W. Chen, Y. Tang, B. Aguila, Y. Pan, A. Zheng, Z. Yang, L. Wojtas and S. Ma, *Matter*, 2020, **2**, 416–427.
61 J. Qi, W. Zhang and R. Cao, *Adv. Energy Mater.*, 2018, **8**, 1701620.
62 L. Stegbauer, K. Schwinghammer and B. V. Lotsch, *Chem. Sci.*, 2014, **5**, 2789–2793.
63 V. S. Vyas, F. Haase, L. Stegbauer, G. Savasci, F. Podjaski, C. Ochsenfeld and B. V. Lotsch, *Nat. Commun.*, 2015, **6**, 8508.
64 R. Chen, Y. Wang, Y. Ma, A. Mal, X.-Y. Gao, L. Gao, L. Qiao, X.-B. Li, L.-Z. Wu and C. Wang, *Nat. Commun.*, 2021, **12**, 1354.
65 W. Li, X. Huang, T. Zeng, Y. A. Liu, W. Hu, H. Yang, Y. B. Zhang and K. Wen, *Angew. Chem., Int. Ed.*, 2021, **60**, 1869–1874.
66 Z. Li, T. Deng, S. Ma, Z. Zhang, G. Wu, J. Wang, Q. Li, H. Xia, S.-W. Yang and X. Liu, *J. Am. Chem. Soc.*, 2023, **145**, 8364–8374.
67 J. L. Sheng, H. Dong, X. B. Meng, H. L. Tang, Y. H. Yao, D. Q. Liu, L. L. Bai, F. M. Zhang, J. Z. Wei and X. J. Sun, *ChemCatChem*, 2019, **11**, 2313–2319.
68 E. Jin, Z. Lan, Q. Jiang, K. Geng, G. Li, X. Wang and D. Jiang, *Chem*, 2019, **5**, 1632–1647.
69 Y. Li, L. Yang, H. He, L. Sun, H. Wang, X. Fang, Y. Zhao, D. Zheng, Y. Qi and Z. Li, *Nat. Commun.*, 2022, **13**, 1355.
70 C. Mo, M. Yang, F. Sun, J. Jian, L. Zhong, Z. Fang, J. Feng and D. Yu, *Advanced Science*, 2020, **7**, 1902988.
71 S. Li, R. Ma, S. Xu, T. Zheng, G. Fu, Y. Wu, Z. Liao, Y. Kuang, Y. Hou and D. Wang, *J. Am. Chem. Soc.*, 2022, **144**, 13953–13960.
72 G. Fu, D. Yang, S. Xu, S. Li, Y. Zhao, H. Yang, D. Wu, P. S. Petkov, Z.-A. Lan, X. Wang and T. Zhang, *J. Am. Chem. Soc.*, 2024, **146**, 1318–1325.
73 J. Cheng, Y. Wu, W. Zhang, J. Zhang, L. Wang, M. Zhou, F. Fan, X. Wu and H. Xu, *Adv. Mater.*, 2024, **36**, 2305313.
74 J. Yang, A. Acharjya, M. Y. Ye, J. Rabeah, S. Li, Z. Kochovski, S. Youk, J. Roeser, J. Grüneberg and C. Penschke, *Angew. Chem., Int. Ed.*, 2021, **60**, 19797–19803.
75 Y. Zhong, W. Dong, S. Ren and L. Li, *Adv. Mater.*, 2024, **36**, 2308251.
76 C. Li, J. Liu, H. Li, K. Wu, J. Wang and Q. Yang, *Nat. Commun.*, 2022, **13**, 2357.
77 T. Sun, S. Li, L. Zhang and Y. Xu, *Angew. Chem., Int. Ed.*, 2023, **62**, e202306617.
78 S. Wei, F. Zhang, W. Zhang, P. Qiang, K. Yu, X. Fu, D. Wu, S. Bi and F. Zhang, *J. Am. Chem. Soc.*, 2019, **141**, 14272–14279.

79 Y. Zang, R. Wang, P.-P. Shao, X. Feng, S. Wang, S.-Q. Zang and T. C. Mak, *J. Mater. Chem. A*, 2020, **8**, 25094–25100.
80 M. Wang, H. Lv, B. Dong, W. He, D. Yuan, X. Wang and R. Wang, *Angew. Chem., Int. Ed.*, 2024, **63**, e202401969.
81 G. Liu, G. Pan, Q. Dang, R. Li, L. Li, C. Yang and Y. Yu, *ChemCatChem*, 2022, **14**, e202101800.
82 J. Li, J. Zhou, X. H. Wang, C. Guo, R. H. Li, H. Zhuang, W. Feng, Y. Hua and Y. Q. Lan, *Angew. Chem., Int. Ed.*, 2024, **136**, e202411721.
83 C.-C. Li, M.-Y. Gao, X.-J. Sun, H.-L. Tang, H. Dong and F.-M. Zhang, *Appl. Catal., B*, 2020, **266**, 118586.
84 Y. Wang, Z. Hu, W. Wang, H. He, L. Deng, Y. Zhang, J. Huang, N. Zhao, G. Yu and Y.-N. Liu, *Chem. Sci.*, 2021, **12**, 16065–16073.
85 K. Gottschling, G. k. Savasci, H. Vignolo-González, S. Schmidt, P. Mauker, T. Banerjee, P. Rovó, C. Ochsenfeld and B. V. Lotsch, *J. Am. Chem. Soc.*, 2020, **142**, 12146–12156.
86 F. M. Zhang, J. L. Sheng, Z. D. Yang, X. J. Sun, H. L. Tang, M. Lu, H. Dong, F. C. Shen, J. Liu and Y. Q. Lan, *Angew. Chem., Int. Ed.*, 2018, **57**, 12106–12110.
87 H. Wang, C. Qian, J. Liu, Y. Zeng, D. Wang, W. Zhou, L. Gu, H. Wu, G. Liu and Y. Zhao, *J. Am. Chem. Soc.*, 2020, **142**, 4862–4871.
88 C. Lin, C. Han, L. Gong, X. Chen, J. Deng, D. Qi, Y. Bian, K. Wang and J. Jiang, *Catal. Sci. Technol.*, 2021, **11**, 2616–2621.
89 T. Zhou, L. Wang, X. Huang, J. Unruangsri, H. Zhang, R. Wang, Q. Song, Q. Yang, W. Li and C. Wang, *Nat. Commun.*, 2021, **12**, 3934.
90 X. A. Li, Z. Z. Liang, Y. C. Zhou, J. F. Huang, X. L. Wang, L. M. Xiao and J. M. Liu, *Aggregate*, 2024, **5**, e442.
91 B. B. Luan, X. Chu, Y. Wang, X. Qiao, Y. Jiang and F. M. Zhang, *Adv. Mater.*, 2024, **36**, 2412653.
92 M. R. Rao, Y. Fang, S. De Feyter and D. F. Perepichka, *J. Am. Chem. Soc.*, 2017, **139**, 2421–2427.
93 W. Dong, Z. Qin, K. Wang, Y. Xiao, X. Liu, S. Ren and L. Li, *Angew. Chem., Int. Ed.*, 2023, **62**, e202216073.
94 Y. Zhong, W. Dong, S. Ren and L. Li, *Adv. Mater.*, 2024, **36**, e2308251.
95 X. Zhang, C. Gao, Y. Zhou, R. Chen, X. Guan, Z. Shen, B. Hu and Q.-H. Xu, *Sci. China:Chem.*, 2025, 1–9.
96 H. Dong and F. M. Zhang, *Chin. J. Struct. Chem.*, 2024, **43**, 100304.
97 Y. Fu, X. Zhu, L. Huang, X. Zhang, F. Zhang and W. Zhu, *Appl. Catal., B*, 2018, **239**, 46–51.
98 D. H. Streater, E. R. Kennehan, D. Wang, C. Fiankor, L. Chen, C. Yang, B. Li, D. Liu, F. Ibrahim and I. Hermans, *J. Am. Chem. Soc.*, 2024, **146**, 4489–4499.
99 J.-X. Cui, L.-J. Wang, L. Feng, B. Meng, Z.-Y. Zhou, Z.-M. Su, K. Wang and S. Liu, *J. Mater. Chem. A*, 2021, **9**, 24895–24902.
100 X. Yu, K. Gong, S. Tian, G. Gao, J. Xie and X.-H. Jin, *J. Mater. Chem. A*, 2023, **11**, 5627–5635.
101 L. j. Wang, R. l. Wang, X. Zhang, J. l. Mu, Z. y. Zhou and Z. m. Su, *ChemSusChem*, 2020, **13**, 2973–2980.
102 L. Ai, W. Li, Q. Wang, F. Cui and G. Jiang, *ChemCatChem*, 2022, **14**, e202200935.
103 Y.-N. Gong, W. Zhong, Y. Li, Y. Qiu, L. Zheng, J. Jiang and H.-L. Jiang, *J. Am. Chem. Soc.*, 2020, **142**, 16723–16731.
104 J. Ding, X. Guan, J. Lv, X. Chen, Y. Zhang, H. Li, D. Zhang, S. Qiu, H.-L. Jiang and Q. Fang, *J. Am. Chem. Soc.*, 2023, **145**, 3248–3254.
105 Y. Xu, J. P. Dong, L. Wang, R. L. Geng, R. Wang, Y. N. Si, S. Q. Zang and T. C. W. Mak, *Angew. Chem., Int. Ed.*, 2025, e202501391.
106 W. Lin, F. Lin, J. Lin, Z. Xiao, D. Yuan and Y. Wang, *J. Am. Chem. Soc.*, 2024, **146**, 16229–16236.
107 Z. Fu, X. Wang, A. M. Gardner, X. Wang, S. Y. Chong, G. Neri, A. J. Cowan, L. Liu, X. Li, A. Vogel and A. I. Cooper, *Chem. Sci.*, 2020, **11**, 543–550.
108 W. Zhong, R. Sa, L. Li, Y. He, L. Li, J. Bi, Z. Zhuang, Y. Yu and Z. Zou, *J. Am. Chem. Soc.*, 2019, **141**, 7615–7621.
109 L. Ran, Z. Li, B. Ran, J. Cao, Y. Zhao, T. Shao, Y. Song, M. K. Leung, L. Sun and J. Hou, *J. Am. Chem. Soc.*, 2022, **144**, 17097–17109.
110 M. Lu, Q. Li, J. Liu, F.-M. Zhang, L. Zhang, J.-L. Wang, Z.-H. Kang and Y.-Q. Lan, *Appl. Catal., B*, 2019, **254**, 624–633.
111 Q. Zhang, S. Gao, Y. Guo, H. Wang, J. Wei, X. Su, H. Zhang, Z. Liu and J. Wang, *Nat. Commun.*, 2023, **14**, 1147.
112 S. Yang, R. Sa, H. Zhong, H. Lv, D. Yuan and R. Wang, *Adv. Funct. Mater.*, 2022, **32**, 2110694.
113 H. Lv, P. Li, X. Li, A. Chen, R. Sa, H. Zhu and R. Wang, *Chem. Eng. J.*, 2023, **451**, 138745.
114 X. Lan, H. Li, Y. Liu, Y. Zhang, T. Zhang and Y. Chen, *Angew. Chem.*, 2024, e202407092.
115 J. Wang, W. Zhu, F. Meng, G. Bai, Q. Zhang and X. Lan, *ACS Catal.*, 2023, **13**, 4316–4329.
116 K. Guo, X. Zhu, L. Peng, Y. Fu, R. Ma, X. Lu, F. Zhang, W. Zhu and M. Fan, *Chem. Eng. J.*, 2021, **405**, 127011.
117 Z. Liu, Y. Huang, S. Chang, X. Zhu, Y. Fu, R. Ma, X. Lu, F. Zhang, W. Zhu and M. Fan, *Sustainable Energy Fuels*, 2021, **5**, 2871–2876.
118 S. Dong, Z. Tan, Q. Chen, G. Huang, L. Wu and J. Bi, *J. Colloid Interface Sci.*, 2022, **628**, 573–582.
119 M. Lu, M. Zhang, J. Liu, T.-Y. Yu, J.-N. Chang, L.-J. Shang, S.-L. Li and Y.-Q. Lan, *J. Am. Chem. Soc.*, 2022, **144**, 1861–1871.
120 B. Zhang, H. Li, Y. Kang, K. Yang, H. Liu, Y. Zhao and S. Qiao, *Adv. Funct. Mater.*, 2025, **35**, 2416958.
121 M. Zhang, M. Lu, Z. L. Lang, J. Liu, M. Liu, J. N. Chang, L. Y. Li, L. J. Shang, M. Wang, S. L. Li and Y. Q. Lan, *Angew. Chem.*, 2020, **132**, 6562–6568.
122 L. Wang, G. Huang, L. Zhang, R. Lian, J. Huang, H. She, C. Liu and Q. Wang, *J. Energy Chem.*, 2022, **64**, 85–92.
123 Y. Wang, Z. Hu, W. Wang, Y. Li, H. He, L. Deng, Y. Zhang, J. Huang, N. Zhao and G. Yu, *Appl. Catal., B*, 2023, **327**, 122419.
124 X. An, J. Bian, K. Zhu, R. Liu, H. Liu and J. Qu, *Chem. Eng. J.*, 2022, **442**, 135279.
125 L. Zou, R. Sa, H. Zhong, H. Lv, X. Wang and R. Wang, *ACS Catal.*, 2022, **12**, 3550–3557.
126 K. H. Do, D. P. Kumar, A. P. Rangappa, J. Lee, S. Yun and T. K. Kim, *J. Mater. Chem. A*, 2023, **11**, 8392–8403.

127 J. Qiu, Y. Zheng, L. Wang, M. Liu, L. Tian, X. Yu, X. An and G. Lv, *J. Mater. Chem. A*, 2023, **11**, 4572–4578.
128 J. Wang, Y. Yu, J. Cui, X. Li, Y. Zhang, C. Wang, X. Yu and J. Ye, *Appl. Catal., B*, 2022, **301**, 120814.
129 R.-G. Yang, Y.-M. Fu, H.-N. Wang, D.-P. Zhang, Z. Zhou, Y.-Z. Cheng, X. Meng, Y.-O. He and Z.-M. Su, *Chem. Eng. J.*, 2022, **450**, 138040.
130 H. Lin, Y. Liu, Z. Wang, L. Ling, H. Huang, Q. Li, L. Cheng, Y. Li, J. Zhou and K. Wu, *Angew. Chem.*, 2022, **134**, e202214142.
131 Z. Zhao, D. Zheng, M. Guo, J. Yu, S. Zhang, Z. Zhang and Y. Chen, *Angew. Chem., Int. Ed.*, 2022, **61**, e202200261.
132 Y. N. Gong, J. H. Mei, W. J. Shi, J. W. Liu, D. C. Zhong and T. B. Lu, *Angew. Chem., Int. Ed.*, 2024, **63**, e202318735.
133 A. Dey, J. Pradhan, S. Biswas, F. Ahamed Rahimi, K. Biswas and T. K. Maji, *Angew. Chem., Int. Ed.*, 2024, **136**, e202315596.
134 S. Wan, F. Gándara, A. Asano, H. Furukawa, A. Saeki, S. K. Dey, L. Liao, M. W. Ambrogio, Y. Y. Botros and X. Duan, *Chem. Mater.*, 2011, **23**, 4094–4097.
135 Y. Xiang, W. Dong, P. Wang, S. Wang, X. Ding, F. Ichihara, Z. Wang, Y. Wada, S. Jin and Y. Weng, *Appl. Catal., B*, 2020, **274**, 119096.
136 J.-X. Cui, Y.-M. Fu, B. Meng, J. Zhou, Z.-Y. Zhou, S.-M. Liu and Z.-M. Su, *J. Mater. Chem. A*, 2022, **10**, 13418–13427.
137 Y. Zhang, L. Cao, G. Bai and X. Lan, *Small*, 2023, **19**, 2300035.
138 M. Kou, W. Liu, Y. Wang, J. Huang, Y. Chen, Y. Zhou, Y. Chen, M. Ma, K. Lei and H. Xie, *Appl. Catal., B*, 2021, **291**, 120146.
139 W. Tu, Y. Yang, C. Chen, T. Zhou, T. Li, H. Wang, S. Wu, Y. Zhou, D. O'Hare and Z. Zou, *Small Struct.*, 2023, **4**, 2200233.
140 B. Han, X. Ou, Z. Zhong, S. Liang, H. Deng and Z. Lin, *Small*, 2020, **16**, 2002985.
141 R. Chen, J.-L. Shi, Y. Ma, G. Lin, X. Lang and C. Wang, *Angew. Chem., Int. Ed.*, 2019, **58**, 6430–6434.
142 Z. Liu, Q. Su, P. Ju, X. Li, G. Li, Q. Wu and B. Yang, *Chem. Commun.*, 2020, **56**, 766–769.
143 S. Yang, X. Li, Y. Qin, Y. Cheng, W. Fan, X. Lang, L. Zheng and Q. Cao, *ACS Appl. Mater. Interfaces*, 2021, **13**, 29471–29481.
144 Y. Fang, Y. Liu, H. Huang, J. Sun, J. Hong, F. Zhang, X. Wei, W. Gao, M. Shao, Y. Guo, Q. Tang and Y. Liu, *Nat. Commun.*, 2024, **15**, 4856.
145 J.-C. Liu, C. Tuo, W.-Y. Xiao, M.-Y. Qi, Y. Yusran, Z.-T. Wang, H. Li, C.-S. Guo, J.-L. Song, S.-L. Qiu, Y.-J. Xu and Q. Fang, *Angew. Chem., Int. Ed.*, 2024, e202416240.
146 W. Hao, D. Chen, Y. Li, Z. Yang, G. Xing, J. Li and L. Chen, *Chem. Mater.*, 2019, **31**, 8100–8105.
147 Q. Li, X. Lan, G. An, L. Ricardez-Sandoval, Z. Wang and G. Bai, *ACS Catal.*, 2020, **10**, 6664–6675.
148 X. Li, Y. Wang, F. Zhang and X. Lang, *J. Colloid Interface Sci.*, 2023, **648**, 683–692.
149 F. Huang, Y. Wang, X. Dong and X. Lang, *Sci. China:Chem.*, 2023, **66**, 3290–3296.
150 X. Dong, F. Zhang, Y. Wang, F. Huang and X. Lang, *Appl. Catal., B*, 2024, **345**, 123660.
151 P.-F. Wei, M.-Z. Qi, Z.-P. Wang, S.-Y. Ding, W. Yu, Q. Liu, L.-K. Wang, H.-Z. Wang, W.-K. An and W. Wang, *J. Am. Chem. Soc.*, 2018, **140**, 4623–4631.
152 S. Bi, P. Thiruvengadam, S. Wei, W. Zhang, F. Zhang, L. Gao, J. Xu, D. Wu, J.-S. Chen and F. Zhang, *J. Am. Chem. Soc.*, 2020, **142**, 11893–11900.
153 Y. Qian, D. Li, Y. Han and H.-L. Jiang, *J. Am. Chem. Soc.*, 2020, **142**, 20763–20771.
154 Z. Li, Y. Zhi, P. Shao, H. Xia, G. Li, X. Feng, X. Chen, Z. Shi and X. Liu, *Appl. Catal., B*, 2019, **245**, 334–342.
155 H. Liu, C. Li, H. Li, Y. Ren, J. Chen, J. Tang and Q. Yang, *ACS Appl. Mater. Interfaces*, 2020, **12**, 20354–20365.
156 H. Shan, D. Cai, X. Zhang, Q. Zhu, P. Qin and J. Baeyens, *Chem. Eng. J.*, 2022, **432**, 134288.
157 Z. Li, S. Han, C. Li, P. Shao, H. Xia, H. Li, X. Chen, X. Feng and X. Liu, *J. Mater. Chem. A*, 2020, **8**, 8706–8715.
158 Y. Yang, H. Niu, L. Xu, H. Zhang and Y. Cai, *Appl. Catal., B*, 2020, **269**, 118799.
159 M. Bhadra, S. Kandambeth, M. K. Sahoo, M. Addicoat, E. Balaraman and R. Banerjee, *J. Am. Chem. Soc.*, 2019, **141**, 6152–6156.
160 H. Chen, W. Liu, A. Laemont, C. Krishnaraj, X. Feng, F. Rohman, M. Meledina, Q. Zhang, R. Van Deun, K. Leus and P. Van Der Voort, *Angew. Chem., Int. Ed.*, 2021, **60**, 10820–10827.
161 W. Dong, Y. Yang, Y. Xiang, S. Wang, P. Wang, J. Hu, L. Rao and H. Chen, *Green Chem.*, 2021, **23**, 5797–5805.
162 A. López-Magano, A. E. Platero-Prats, S. Cabrera, R. Mas-Ballesté and J. Alemán, *Appl. Catal., B*, 2020, **272**, 119027.
163 Z. Almansaf, J. Hu, F. Zanca, H. R. Shahsavari, B. Kampmeyer, M. Tsuji, K. Maity, V. Lomonte, Y. Ha, P. Mastrorilli, S. Todisco, M. Benamara, R. Oktavian, A. Mirjafari, P. Z. Moghadam, A. R. Khosropour and H. Beyzavi, *ACS Appl. Mater. Interfaces*, 2021, **13**, 6349–6358.
164 A. Jati, K. Dey, M. Nurhuda, M. A. Addicoat, R. Banerjee and B. Maji, *J. Am. Chem. Soc.*, 2022, **144**, 7822–7833.
165 S. Shi, W. Liu, Y. Li, S. Lu, H. Zhu, M. Du, X. Chen and F. Duan, *J. Colloid Interface Sci.*, 2024, **655**, 611–621.
166 Y. Gao, S. Li, L. Gong, J. Li, D. Qi, N. Liu, Y. Bian and J. Jiang, *Angew. Chem., Int. Ed.*, 2024, **63**, e202404156.
167 J.-L. Shi, R. Chen, H. Hao, C. Wang and X. Lang, *Angew. Chem., Int. Ed.*, 2020, **59**, 9088–9093.
168 K. Feng, H. Hao, F. Huang, X. Lang and C. Wang, *Mater. Chem. Front.*, 2021, **5**, 2255–2260.
169 G. Lu, X. Huang, Y. Li, G. Zhao, G. Pang and G. Wang, *J. Energy Chem.*, 2020, **43**, 8–15.
170 K. Zhang, G. Lu, Z. Xi, Y. Li, Q. Luan and X. Huang, *Chin. Chem. Lett.*, 2021, **32**, 2207–2211.
171 Q. Qin, Z.-H. Xia, W.-Q. Liu, H.-Y. Chen and D.-B. Kuang, *Small*, 2024, **20**, 2402410.
172 X. Zhao, A. Li, D. Yang, T.-Y. Qiu, Z. Zhao, S.-L. Wang, X. Mu and H.-Q. Tan, *J. Colloid Interface Sci.*, 2024, **653**, 67–76.
173 C. Krishnaraj, H. Sekhar Jena, L. Bourda, A. Laemont, P. Pachfule, J. Roeser, C. V. Chandran, S. Borgmans, S. M. J. Rogge, K. Leus, C. V. Stevens, J. A. Martens,

V. Van Speybroeck, E. Breynaert, A. Thomas and P. Van Der Voort, *J. Am. Chem. Soc.*, 2020, **142**, 20107–20116.

174 J.-N. Chang, Q. Li, J.-W. Shi, M. Zhang, L. Zhang, S. Li, Y. Chen, S.-L. Li and Y.-Q. Lan, *Angew. Chem., Int. Ed.*, 2023, **62**, e202218868.

175 L. Zhai, Z. Xie, C.-X. Cui, X. Yang, Q. Xu, X. Ke, M. Liu, L.-B. Qu, X. Chen and L. Mi, *Chem. Mater.*, 2022, **34**, 5232–5240.

176 F. Liu, P. Zhou, Y. Hou, H. Tan, Y. Liang, J. Liang, Q. Zhang, S. Guo, M. Tong and J. Ni, *Nat. Commun.*, 2023, **14**, 4344.

177 C. Qin, X. Wu, L. Tang, X. Chen, M. Li, Y. Mou, B. Su, S. Wang, C. Feng, J. Liu, X. Yuan, Y. Zhao and H. Wang, *Nat. Commun.*, 2023, **14**, 5238.

178 Y. Mou, X. Wu, C. Qin, J. Chen, Y. Zhao, L. Jiang, C. Zhang, X. Yuan, E. Huixiang Ang and H. Wang, *Angew. Chem., Int. Ed.*, 2023, **62**, e202309480.

179 Y. Hou, P. Zhou, F. Liu, Y. Lu, H. Tan, Z. Li, M. Tong and J. Ni, *Angew. Chem., Int. Ed.*, 2024, **63**, e202318562.

180 H. Yu, F. Zhang, Q. Chen, P.-K. Zhou, W. Xing, S. Wang, G. Zhang, Y. Jiang and X. Chen, *Angew. Chem., Int. Ed.*, 2024, **63**, e202402297.

181 H. Wang, C. Yang, F. Chen, G. Zheng and Q. Han, *Angew. Chem., Int. Ed.*, 2022, **61**, e202202328.

182 M. Kou, Y. Wang, Y. Xu, L. Ye, Y. Huang, B. Jia, H. Li, J. Ren, Y. Deng, J. Chen, Y. Zhou, K. Lei, L. Wang, W. Liu, H. Huang and T. Ma, *Angew. Chem., Int. Ed.*, 2022, **61**, e202200413.

183 T. Yang, Y. Wang, Y. Chen, X. Peng, H. Zhang and A. Kong, *CrystEngComm*, 2023, **25**, 4511–4520.

184 W.-K. Han, H.-S. Lu, J.-X. Fu, X. Liu, X. Zhu, X. Yan, J. Zhang, Y. Jiang, H. Dong and Z.-G. Gu, *Chem. Eng. J.*, 2022, **449**, 137802.

185 M. Wu, Z. Shan, J. Wang, T. Liu and G. Zhang, *Chem. Eng. J.*, 2023, **454**, 140121.

186 Q. Zhi, W. Liu, R. Jiang, X. Zhan, Y. Jin, X. Chen, X. Yang, K. Wang, W. Cao, D. Qi and J. Jiang, *J. Am. Chem. Soc.*, 2022, **144**, 21328–21336.

187 Y. Liu, L. Li, H. Tan, N. Ye, Y. Gu, S. Zhao, S. Zhang, M. Luo and S. Guo, *J. Am. Chem. Soc.*, 2023, **145**, 19877–19884.

188 Y. Zhang, J. Qiu, B. Zhu, M. V. Fedin, B. Cheng, J. Yu and L. Zhang, *Chem. Eng. J.*, 2022, **444**, 136584.

189 Y. Yang, J. Liu, M. Gu, B. Cheng, L. Wang and J. Yu, *Appl. Catal., B*, 2023, **333**, 122780.

190 W. Ren, Q. Chang, N. Li, J. Yang and S. Hu, *Chem. Eng. J.*, 2023, **451**, 139035.

191 J.-Y. Yue, Z.-X. Pan, P. Yang and B. Tang, *ACS Mater. Lett.*, 2024, **6**, 3932–3940.

192 X. Ma, S. Li, Y. Gao, N. Li, Y. Han, H. Pan, Y. Bian and J. Jiang, *Adv. Funct. Mater.*, 2024, **34**, 2409913.

193 Y. Zheng, T. Gao, S. Chen, C. T. J. Ferguson, K. A. I. Zhang, F. Fang, Y. Shen, N. A. Khan, L. Wang and L. Ye, *Compos. Commun.*, 2022, **36**, 101390.

194 G. Xia, J. Qiu, L. Zhang, D. Dai and J. Yao, *Colloids Surf., A*, 2023, **664**, 131124.

195 Y. Yang, Y. Li, X. Ma, L. Xie, D. Lv, L. Jiang, J. He, D. Chen and J. Wang, *Catal. Sci. Technol.*, 2023, **13**, 5599–5609.

196 Y. Shao, D. You, Y. Wan, Q. Cheng and Z. Pan, *Dalton Trans.*, 2023, **52**, 11272–11284.